NeuroImage 263 (2022) 119592

Contents lists available at ScienceDirect

NeuroImage

journal homepage: www.elsevier.com/locate/neuroimage

Space-time resolved inference-based neurophysiological process imaging: Application to resting-state alpha rhythm

Yun Zhao[a], Mario Boley[a], Andria Pelentritou[b,c], Philippa J. Karoly[d,e], Dean R. Freestone[e,f], Yueyang Liu[a], Suresh Muthukumaraswamy[g], William Woods[h], David Liley[b,e,h], Levin Kuhlmann[a,e,*]

[a] Department of Data Science and Artificial Intelligence, Faculty of Information Technology, Monash University, Clayton, Victoria, Australia
[b] Swinburne University of Technology, Hawthorn, Australia
[c] Laboratoire de Recherche en Neuroimagerie (LREN), University Hospital (CHUV) and University of Lausanne (UNIL), Lausanne, Switzerland
[d] Department of Biomedical Engineering, The University of Melbourne, Parkville, Australia
[e] Department of Medicine-St Vincent's Hospital, The University of Melbourne, Parkville, Australia
[f] Seer Medical Pty Ltd, Melbourne, Australia
[g] School of Pharmacy, University of Auckland, New Zealand
[h] School of Health Sciences, Swinburne University of Technology, Hawthorn, Australia

ARTICLE INFO

Keywords:
Brain imaging
Neural mass model
Kalman filtering
Parameter estimation
Alpha rhythm
Resting state

ABSTRACT

Neural processes are complex and difficult to image. This paper presents a new space-time resolved brain imaging framework, called Neurophysiological Process Imaging (NPI), that identifies neurophysiological processes within cerebral cortex at the macroscopic scale. By fitting uncoupled neural mass models to each electromagnetic source time-series using a novel nonlinear inference method, population averaged membrane potentials and synaptic connection strengths are efficiently and accurately inferred and imaged across the whole cerebral cortex at a resolution afforded by source imaging. The efficiency of the framework enables return of the augmented source imaging results overnight using high performance computing. This suggests it can be used as a practical and novel imaging tool. To demonstrate the framework, it has been applied to resting-state magnetoencephalographic source estimates. The results suggest that endogenous inputs to cingulate, occipital, and inferior frontal cortex are essential modulators of resting-state alpha power. Moreover, endogenous input and inhibitory and excitatory neural populations play varied roles in mediating alpha power in different resting-state sub-networks. The framework can be applied to arbitrary neural mass models and has broad applicability to image neural processes of different brain states.

1. Introduction

A long-standing goal in neuroscience is to image the human brain's neural processes to understand the patterns of neural activity that give rise to mental processes and behaviours. Modern human neuroimaging methods have made significant progress towards unlocking these processes. Functional magnetic resonance imaging (fMRI), the most commonly used functional neuroimaging technique, has revealed fundamental insights into spontaneous and task-dependant brain activity by imaging the blood oxygenation changes related to the metabolic processes of neurons (Logothetis et al., 2001). Electroencephalography (EEG) and magnetoencephalography (MEG) have been used to study oscillatory neural activity by measuring the electrical and magnetic fields induced by source currents within the brain (Nunez and Srinivasan, 2006). However, both fMRI and M/EEG do not provide a direct measure of the neurophysiological variables that generate these source currents or blood oxygenation changes (Cohen, 2017; Logothetis, 2003). In particular, it is well known that cellular membrane potentials and post-synaptic potentials are critical neurophysiological variables involved in dynamic information processing in the brain (Kandel et al., 2000) and the generation of macroscopic currents (Nunez and Srinivasan, 2006) and modulation of blood-oxygenation signals (Logothetis et al., 2001). These neurophysiological variables have long been the purview of cellular and systems neuroscience and have afforded the elucidation of the neural processes underlying many brain functions (Kandel et al., 2000). While there have been advances with multi-photon imaging of neural tissue (Hoover and Squier, 2013) and magnetic resonance spectroscopy to image specific neurotransmitter changes (Novotny Jr et al., 2003), work remains to be

* Corresponding author.
E-mail address: levin.kuhlmann@monash.edu (L. Kuhlmann).

https://doi.org/10.1016/j.neuroimage.2022.119592.
Received 26 April 2022; Received in revised form 28 July 2022; Accepted 24 August 2022
Available online 27 August 2022.

completed to provide efficient space-time resolved imaging of the aforementioned neurophysiological variables across the whole human brain.

Computational models provide an alternative to capture neural processes by abstracting latent population averaged neurophysiological variables in mathematical models (Deco et al., 2008). Neural mass models (NMMs) are neural population-level models used in studying neural oscillations by modelling the activity of groups of excitatory and inhibitory neurons within a brain region and approximating the averaged properties and interactions (Deco et al., 2008). The combination of such models and model inversion, which estimates neurophysiological variables in the model from data (Schiff, 2012), provides a powerful way to infer neural processes from functional neuroimaging recordings. Dynamic causal modelling (DCM) has been one of the principal frameworks that study neural processes in this way (Friston et al., 2019; Kiebel et al., 2008). Specifically, DCM focuses on the task-dependant effective connectivity amongst multiple selected brain regions. Given the challenge of model inversion for highly complex systems like the brain, there is hitherto little work done to image space-time resolved brain-wide neurophysiological processes. Model inversion that can scale to the whole brain at a spatial resolution commensurate with current human neuroimaging techniques, is a computationally formidable challenge for complex non-linear neural models (Schiff, 2012). Most model inversion methods that are efficient and therefore scalable, usually rely on linearising nonlinear neural models and are therefore less accurate (Freestone et al., 2017; Prando et al., 2020). On the other hand, inversion methods that are easy to implement, like sampling techniques, are usually computationally demanding and therefore less scalable (Abeysuriya and Robinson, 2016; Kuhlmann et al., 2016). Thus, existing methods are not suitable for space-time resolved whole-brain imaging with a reasonable computational time budget and acceptable estimation accuracy.

This paper presents a novel whole-brain imaging framework, Neurophysiological Processes Imaging (NPI), that extends existing electromagnetic source imaging methods (Van Veen et al., 1997) to infer and image neurophysiological variables in a space-time resolved manner. The framework is demonstrated by applying it to human MEG resting-state alpha (8–12 Hz) rhythm data and inferring and imaging population mean (i.e., spatial, not time averaged) membrane potentials and population mean synaptic strengths of cerebral-cortical excitatory and inhibitory neuronal populations at the spatial and temporal resolutions afforded by MEG (6 mm spaced sources, 400 Hz sampling rate). The framework allows for the general application of NMMs containing an arbitrary combination of interconnected excitatory and inhibitory populations and involves an efficient time-domain Bayesian inference method derived specifically for nonlinear NMMs.

Although the accuracy and interpretation of the inferred neurophysiological variables of such a framework depends on the assumed neural model applied in a specific situation (Schiff, 2012), a similar problem is present in standard fMRI analysis where a hemodynamic response function (HRF) is applied even though it is known to depend on various factors and therefore can be modelled in different ways (Aquino et al., 2014). The typical solution to get around these complexities is to apply a canonical HRF to each voxel in the brain, and this has enabled the general application of fMRI to many different neuroscience topics. With this in mind, and akin to DCM for M/EEG (Kiebel et al., 2008), here we present a novel imaging framework using a canonical NMM. In summary, our analysis can be regarded as a form of dynamic causal modelling that can handle thousands of sources or nodes. The reason for this remarkable functionality is that the between-node (i.e., extrinsic) connectivity parameters are replaced by a single extrinsic input to each node, which is estimated from the node's responses. Effectively, this means that we can invert each node separately and finesse the computational complexity of inverting a model of distributed and coupled neuronal responses. Note that we can still estimate within-node (i.e., intrinsic) connectivity amongst populations within a neural mass model. This is potentially important because many applications of dynamic causal modelling focus on intrinsic connectivity as a proxy for neuromodulatory effects and cortical excitation and inhibition balance (Kiebel et al., 2007; Penny et al., 2004). Although not developed in this paper, we anticipate that the ability to estimate intrinsic connectivity throughout the cortex may be an important adjunct to clinical neuroimaging, particularly in psychiatry. In addition, through application of this novel method we consider different ways in which the inferred variables can be imaged and reveal new insights into the resting-state brain and alpha rhythm (Klimesch et al., 2007; Lozano-Soldevilla, 2018).

2. Material and methods

2.1. Framework for inference-based brain neural processes imaging

The proposed framework for quantifying and imaging neurophysiological variables, employs a canonical NMM (Jansen and Rit, 1995), an efficient Bayesian inference method, and multiple statistical analysis schemes that can be applied to any source time-series derived from electromagnetic imaging. Our method involves a fast, semi-analytic solution to handle the propagation of estimates through the non-linear neural model by re-deriving the well-known Bayesian inference method, Kalman filtering using the specific nonlinearities of the model without having to linearise the model around its equilibrium points (Karoly et al., 2018). This method is referred to here as the semi-analytic Kalman filter (AKF) and creates a more accurate and computationally efficient method which allows, in the examples presented here, the modelling of the whole brain with 4714 NMMs, and provides high spatial and temporal resolution imaging (6 mm source spacing, 400 Hz sampling rate). To demonstrate the utility of the framework, we applied it to beamformed MEG recordings of healthy human male subjects (Pelentritou et al., 2020) to investigate the brain-wide neurophysiological processes of eyes-closed resting-state alpha oscillations. Each MEG source time-series derived from beamforming is treated as proportional to the local extracellular dipole current formed by the combination of population averaged excitatory and inhibitory synaptic currents associated with cortical pyramidal cells (Einevoll, 2021; Nunez and Srinivasan, 2006). This combination of synaptic currents is treated as the output of a single NMM, such that one NMM is used per MEG source point to capture its underlying neural dynamics, as shown in Fig. 1a. By effectively inverting the model, estimates of neurophysiological variables can be obtained.

The NMM considered in this framework is illustrated in Fig. 1a. The model has three neural populations: excitatory pyramidal cells (p), spiny stellate excitatory cells (e) and inhibitory interneurons (i), which coarsely imitates the structure of a small patch of cerebral cortex. The pyramidal population is driven by external input, μ, and excites the excitatory and inhibitory interneurons, while the excitatory and inhibitory interneurons provide excitatory and inhibitory feedback, respectively, to the pyramidal population. The external input encodes the neighbouring and distant afferent input to the cortical patch. The state of a neural population is denoted by the population mean membrane potential, V_n. The population averaged connection strength between two neural populations is defined as α_{mn} (presynaptic and postsynaptic neural populations are indexed by m and n), representing lumped connectivities that incorporate average synaptic gain, number of connections, and averaged maximum firing rate of the presynaptic populations. The variables V_n, α_{mn} and μ are the ones being estimated and imaged across the whole brain. To estimate the neurophysiological variables of the NMMs, the AKF was applied to each of an individual's 4714 source time-series obtained from resting eyes-closed MEG data. Below the data and methods used to illustrate inference-based neural process imaging at the individual and group level are described.

2.2. Dataset

The data used herein was collected from a study analysing resting state and anaesthetic-induced power changes in M/EEG signals. Here we

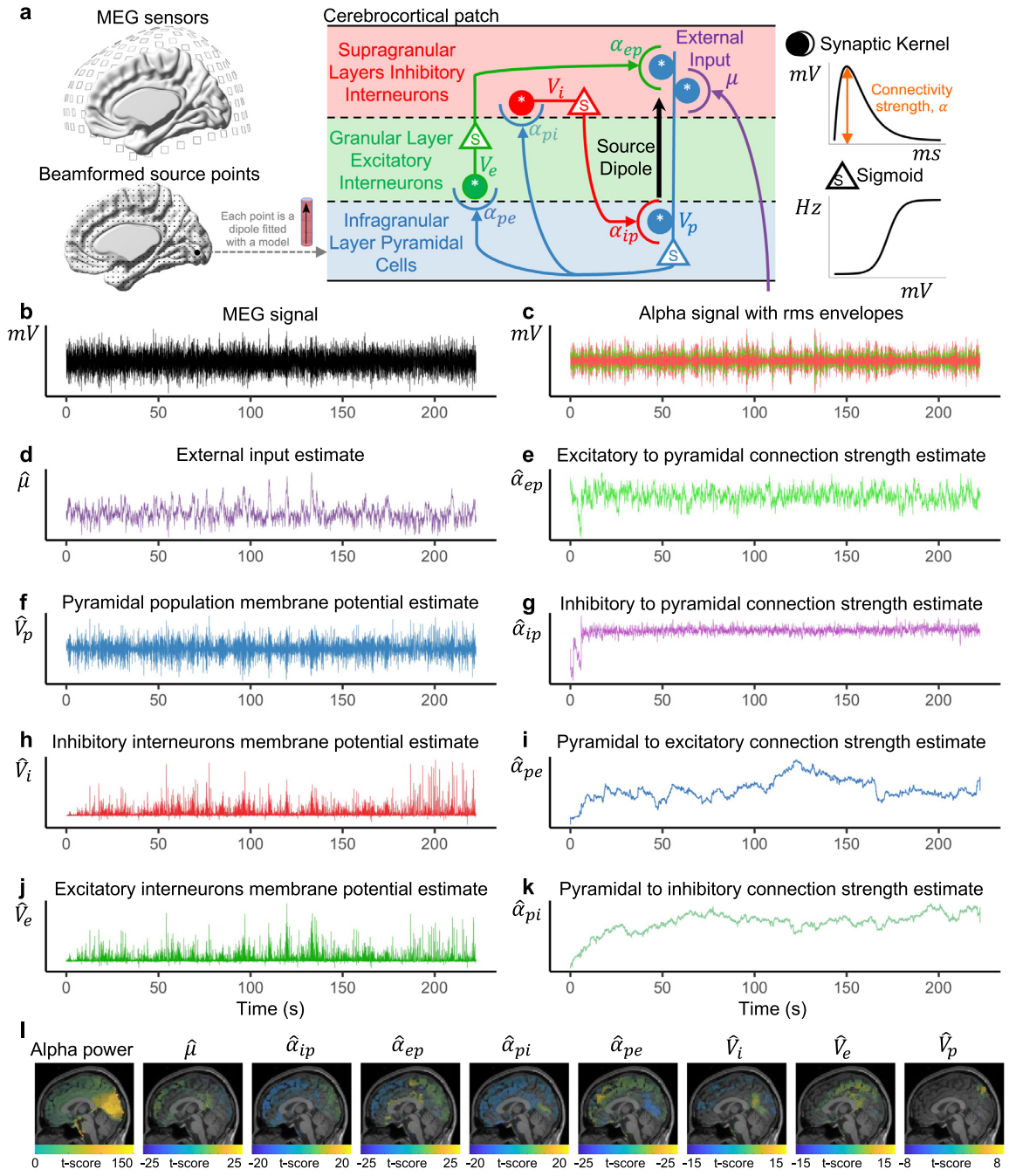

Fig. 1. Schematic and example of space-time resolved inference-based brain imaging of neurophysiological processes. (a) Schematic of brain modelling with the canonical NMM. Each MEG source point was fitted with an NMM. The canonical NMM used in this study contains three populations: pyramidal population, excitatory interneurons, and inhibitory interneurons. (b) A sample recording from a MEG source point located in the occipital lobe of a single subject. (c) Alpha (8–12 Hz) band time-series in red extracted from the sample recording. The corresponding green lines, the rms envelopes, quantify the evolution of the signal power at a slower timescale. (d) – (k) The estimation timeseries of modelled neurophysiological variables obtained by feeding the sample recording into the AKF. (l) An example contrast imaging shows the mean difference of alpha power (rms envelope) and neurophysiological variable estimates between two conditions: occipital strong and weak alpha oscillations. The activated areas in the sub-images represent statistically significant difference was observed after corrections for multiple comparisons (significance level $\alpha = 0.05$).

summarise the key details of the data. For further information see previous papers (Pelentritou et al., 2020, 2018). Twenty-two volunteers were recruited. All participants signed a written informed consent form prior to participation under the approved protocol (Alfred Hospital HREC approval number 260/12). Participants were right-handed adult males, aged between 20 and 40 years (average age was 24 years), and had a body mass index between 18 and 30. Candidates with neurological diseases, mental illnesses, epilepsy, heart disease, respiratory diseases, obstructive sleep apnoea, asthma, motion sickness, and claustrophobia have been excluded from the study. In addition, any recent use of psychoactive drugs or other prescription drugs and any recreational drugs resulted in exclusion. Empirical eyes closed resting-state MEG data collection was carried out in a room shielded from magnetic and electrical interference (Euroshield Ltd., Finland). A 306-channel Elekta Neu-

romag TRIUX MEG system (Elekta Oy, Finland) was used to record brain magnetic field activity at a sampling rate of 1000 Hz. Exactly five minutes of awake, eyes closed resting-state was collected for each participant.

According to the minimum record length after artefact removal, the MEG recordings of all subjects were trimmed to 3.75 min to limit bias to a particular subject in group analysis. An atlas-based version of the linearly constrained minimum variance (LCMV) spatial filtering beamformer was used to project sensor level changes onto sources (Hillebrand et al., 2012; Van Veen et al., 1997). The resulting beamformer weights were normalised to compensate for the inherent depth bias of the method used (Hillebrand et al., 2012). Given that MEG is primarily sensitive to superficial brain structures, it was decided to focus only on analysing the 4714 voxels in the grey matter of cerebral cortex. The beamformed MEG source time-series at each voxel was estimated in the direction of the most power and downsampled to 400 Hz to make neurophysiological variable inference tractable within a reasonable time budget and data storage, while maintaining a relatively high temporal resolution.

2.3. Brain imaging of neurophysiological processes

As described above, at a high level the brain imaging framework aims at efficiently imaging inferred population averaged neurophysiological variables across space and time at the resolution afforded by EEG or MEG inverse source reconstruction methods. In this paper, this is specifically achieved by augmenting MEG inverse source reconstruction methods by inferring neurophysiological variables from derived cortical source activity.

In the presented implementation, the proposed framework utilises a canonical NMM (Jansen and Rit, 1995) to approximate a small cortical patch which contains multiple neuronal populations characterised by population averaged mean membrane potentials, and the interplay between populations quantified by the population averaged synaptic connectivity strengths. While the framework presented here is general enough to use arbitrarily complex NMMs. There are 4714 reconstructed MEG source points in this study and each point was fitted with an NMM. The local neural activity and within-region connections can be captured by each NMM and quantitatively reflected by the model's neurophysiological variables. A novel data-driven Bayesian estimation scheme, namely the AKF, was employed to infer the model's neurophysiological variables from the actual MEG-derived source time-series. Neural processes were then characterised by calculating different statistics based on the neurophysiological variable estimates (details below). Brain imaging was then achieved by projecting the statistics to the corresponding source point location on the MRI and interpolating the values to the neighbouring area. Overall, the proposed framework is a general protocol for working with different modalities of data such as M/EEG source, electrocorticography or local field potential time series. Within the context of this paper, the framework is used to extend MEG source imaging by imaging a variety of statistics to show different aspects of the neurophysiological bases of complex brain states. Most importantly the framework can be used to image reasonably fine-grained spatial and very high-resolution temporal patterns of neural activity.

In this study, the imaging framework has been applied to study the neurophysiological processes underlying the resting-state alpha oscillation. Two types of imaging, contrast imaging and Pearson's correlation-based imaging, were employed to illustrate the neurophysiological processes from two statistical perspectives. To overcome the multiple comparisons problem, a nonparametric permutation test was used to determine the group-level significant voxels across the whole brain for each type of statistical analysis. By projecting the statistics of interest onto the MRI, one can observe the structure-function relationships associated with the inferred neurophysiological variables.

2.4. Neural mass model

It is rational to employ NMMs in the framework to model the macroscopic neural activity measured by M/EEG because the NMM is defined in line with the dynamics of cerebral cortex and the output of the model physiologically corresponds to M/EEG derived source-estimates (Nunez and Srinivasan, 2006). The mathematical formulation given below is general enough to define any large scale NMM that consists of any arbitrary combination of interconnected excitatory and inhibitory neural mass populations. However, the implementation of the local canonical NMM used in this study is derived from the model introduced by Jansen and Rit (Jansen and Rit, 1995) and has been outlined in previous works (Freestone et al., 2011; Karoly et al., 2018; Kuhlmann et al., 2016). The NMM is suitable to model MEG measured at this scale (virtual source dipoles with 6 mm spacing), in line with similar NMMs used to describe EEG or MEG (Aarabi and He, 2014; David and Friston, 2003; Wendling et al., 2002). A single independent NMM was fitted to each MEG source point (4714 models in total). NMMs were not coupled between source points and thereby, neurophysiological variables principally captured the local neural activity within the vicinity of a single cortical source point. The input parameter in Fig. 1a, μ, represents the combination of neighbouring and distant afferent input to the patch approximated by a single NMM.

The model used here is composed of three neural populations (excitatory, inhibitory, and pyramidal). The pyramidal population (in infragranular layers) excites the spiny stellate excitatory population (in granular layer IV) and inhibitory interneurons (in supragranular layers), is driven by endogenous input, is excited by the spiny stellate excitatory population and inhibited by the inhibitory interneurons. Neural populations are described by their time varying mean (spatial, not time averaged) membrane potential, V_n, which is the sum of contributing population mean post-synaptic potentials, V_{mn} (pre-synaptic and post-synaptic neural populations are indexed by m and n) and connected via synapses in which the parameter, α_{mn} quantifies the population averaged connection strength. Principal mathematical symbols and their corresponding interpretations and standard values are summarised in Supplementary Table 1.

In general, a NMM is a time-varying dynamical system and each mean post-synaptic potential, V_{mn}, is defined as two coupled, first-order, ordinary differential equations,

$$\frac{\mathrm{d}V_{mn}}{\mathrm{d}t} = Z_{mn}\frac{\mathrm{d}Z_{mn}}{\mathrm{d}t} = \frac{\alpha_{mn}}{\tau_{mn}}\phi_{mn} - \frac{2}{\tau_{mn}}Z_{mn} - \frac{1}{\tau_{mn}^2}V_{mn} \tag{1}$$

where τ_{mn} is a lumped time constant (membrane average time constant and dendritic tree average time delays) and α_{mn} is a lumped connection strength parameter that incorporates the average synaptic gain, the number of connections and the average maximum firing rate of the presynaptic population. Both time constants and connection strengths are dependant on the type of presynaptic population. For example, GABAergic inhibitory interneurons typically induce a higher amplitude post-synaptic potential with a longer time constant than glutamatergic excitatory cells. ϕ_{mn} encodes the inputs to the population and it may come from external regions, μ, or from other intra-regional populations within the model, $g(V_m)$, where

$$\phi_{mn} = \begin{cases} \mu_m, & \text{if m indexes external inputs} \\ g(V_m), & \text{if m indexes internal inputs} \end{cases} \tag{2}$$

The various populations within the model are linked via the activation function, $g(V_m)$, that describes a mean firing rate as a function of the pre-synaptic population's mean membrane potential. The activation function exploits a sigmoidal relationship (limited firing rate due to refractory period of the neurons) between the mean membrane potential and firing rate of each of the populations. This sigmoidal nonlinearity may take different forms, but for this study the error function form is

used (as it facilitates the derivation of the AKF below) where

$$g(V_m) = \frac{1}{2}\left(\operatorname{erf}\left(\frac{V_m - V_0}{\sqrt{2}\varsigma}\right) + 1\right) \tag{3}$$

The quantity ς describes the slope of the sigmoid or, equivalently, encodes the distribution of depolarizations (Marreiros et al., 2009). The mean firing threshold relative to the mean resting membrane potential is denoted by V_0. The parameters of the sigmoidal activation functions, ς and V_0, are usually assumed to be constants.

Depending on the inputs to a given population, the population averaged membrane potentials can be determined by the formula, $V_n = \sum_m V_{mn}$. Moreover, the postsynaptic potential, V_{mn} defined in the ordinary differential equations can conveniently be written as the convolution of the input firing rate, ϕ_{mn}, with the postsynaptic response kernel, h_{mn},

$$V_{mn}(t) = \alpha_{mn} \int_{-\infty}^{t} h_{mn}(t - t')\phi_{mn}(t')\mathrm{d}t' \tag{4}$$

The post-synaptic response kernels denoted by $h_{mn}(t)$ describe the profile of the post-synaptic membrane potential of population n that is induced by an infinitesimally short pulse from the inputs (like an action potential). The post-synaptic response kernels are parameterised by the time constant τ_{mn} and are given by

$$h_{mn}(t) = \eta(t)\frac{t}{\tau_{mn}}\exp\left(-\frac{t}{\tau_{mn}}\right) \tag{5}$$

where $\eta(t)$ is the Heaviside step function.

In summary, a single NMM component maps from a mean presynaptic firing rate to a post-synaptic potential. The terms of interest in our study are population mean membrane potentials, V_n, and connectivity strengths, α_{mn}, and external cortical input, μ which need to be inferred from the data while fixing the other parameters defined by Jansen and Rit (1995) and Freestone et al. (2014).

Below the NMM is expressed in matrix vector form to facilitate the exposition of the AKF in the following section and to highlight the generality of the framework. The general NMM is linked to the canonical NMM where appropriate. The state vector representing the postsynaptic membrane potentials is defined as

$$\mathbf{x} = \begin{bmatrix} V_1 & Z_1 & \cdots & V_j & Z_j & \cdots V_N & Z_N \end{bmatrix}^\top \tag{6}$$

where the subscript, j, indexes the possible connections between populations in the neural mass. There are two states per population averaged synapse where V_j denotes the mean post-synaptic membrane potential and Z_j denotes the first order derivative of the mean post-synaptic membrane potential. Note that V_j can be interpreted as the vectorisation of V_{mn} and is distinct from V_n. In the context of the implementation of each local canonical NMM, the state vector can be expressed as

$$\mathbf{x} = \begin{bmatrix} V_{ip} & Z_{ip} & V_{pi} & Z_{pi} & V_{pe} & Z_{pe} & V_{ep} & Z_{ep} \end{bmatrix}^\top \tag{7}$$

The general fully interconnected NMM can be expressed in a matrix notation

$$\dot{\mathbf{x}}(t) = \mathbf{A}\mathbf{x}(t) + \mathbf{B}\mathbf{x}(t) \circ \phi(\mathbf{C}\mathbf{x}(t)) \tag{8}$$

The matrix $\mathbf{A}$ encodes the dynamics induced by the membrane time constants. For N synapses, $\mathbf{A}$ has the block diagonal structure

$$\mathbf{A} = \operatorname{diag}\begin{pmatrix} \boldsymbol{\psi}_1 \cdots & \boldsymbol{\psi}_\mathbf{j} & \cdots \boldsymbol{\psi}_\mathbf{N} \end{pmatrix} \tag{9}$$

where

$$\boldsymbol{\psi}_\mathbf{j} = \begin{bmatrix} 0 & 1 \\ -\frac{1}{\tau_{mn}} & -\frac{2}{\tau_{mn}} \end{bmatrix} \tag{10}$$

The matrix $\mathbf{B}$ maps the connectivity gains to the relevant sigmoidal activation function and is of the form

$$\mathbf{B} = \begin{bmatrix} 0 & \cdots & 0 \\ \alpha_1 & & 0 \\ \vdots & \ddots & \vdots \\ 0 & & 0 \\ 0 & \cdots & \alpha_N \end{bmatrix} \tag{11}$$

where α_i are the connection strength parameters in the NMM and can be thought of as the vectorisation of α_{mn}. The vector function $\phi()$ has the following form

$$\phi(\mathbf{C}\mathbf{x}) = \begin{bmatrix} 0 & g(\mathbf{c}_{2,:}\mathbf{x}) & \cdots & 0 & g(\mathbf{c}_{\mathbf{N}-2,:}\mathbf{x}) & 0 \end{bmatrix}^\top \tag{12}$$

where $g()$ is the sigmoid function defined above. The adjacency matrix, $\boldsymbol{C}$, defines the connectivity structure of the model. It is a matrix of zeros and ones that specifies all the connections between neural populations that has the block structure

$$\mathbf{C} = \begin{bmatrix} 0 & 0 & \cdots & 0 & 0 \\ \mathrm{c}_{2,1} & 0 & & \mathrm{c}_{2,\mathrm{N}-1} & 0 \\ \vdots & \vdots & \ddots & \vdots & \vdots \\ 0 & 0 & & 0 & 0 \\ \mathrm{c}_{\mathrm{N},1} & 0 & \cdots & \mathrm{c}_{\mathrm{N},\mathrm{N}-1} & 0 \end{bmatrix} \tag{13}$$

In general, for the AKF derivation below to work only connectivity strengths α_i can be estimated while the other parameters are treated as known constants. The benefit of this approach is that it leads to a highly efficient and scalable estimation algorithm. The connectivity strengths to be estimated can be formed into a parameter vector

$$\boldsymbol{\theta} = \begin{bmatrix} \alpha_1 \ldots & \alpha_i \ldots & \alpha_N \end{bmatrix}^\top \tag{14}$$

In the specific context of implementing the local canonical NMM that only involves the pyramidal, excitatory interneuron and inhibitory interneuron populations, the parameter vector for each canonical NMM can be expressed as.

$$\boldsymbol{\theta} = \begin{bmatrix} \mu & \alpha_{ip} & \alpha_{pi} & \alpha_{pe} & \alpha_{ep} \end{bmatrix}^\top \tag{15}$$

The dynamics for the parameters are modelled as constant

$$\dot{\boldsymbol{\theta}} = 0 \tag{16}$$

however, during estimation they are assumed to follow a random walk. The differential form of the parameter vector facilitates augmenting the parameters to the state vector for estimation purposes. The augmented state space vector is created as

$$\boldsymbol{\xi} = \begin{bmatrix} \mathbf{x}^\top & \boldsymbol{\theta}^\top \end{bmatrix}^\top \tag{17}$$

Accordingly, the matrices $\mathbf{A}_\theta$, $\mathbf{B}_\theta$, and $\mathbf{C}_\theta$ are created based on $\mathbf{A}$, $\mathbf{B}$, and $\mathbf{C}$ to match the augmented state vector.

$$\mathbf{A}_\theta = \begin{bmatrix} \mathbf{A} & 0 \\ 0 & \mathbf{I} \end{bmatrix},\ \mathbf{B}_\theta = \begin{bmatrix} \mathbf{B} & 0 \\ 0 & 0 \end{bmatrix},\ \mathbf{C}_\theta = \begin{bmatrix} \mathbf{C} & 0 \\ 0 & 0 \end{bmatrix} \tag{18}$$

The augmented state space model is of the form

$$\dot{\boldsymbol{\xi}}(t) = \mathbf{A}_\theta\boldsymbol{\xi}(t) + \mathbf{B}_\theta\boldsymbol{\xi}(t) \circ \phi\left(\mathbf{C}_\theta\boldsymbol{\xi}(t)\right) \tag{19}$$

It is necessary to discretise the model with respect to time for estimation purposes. Therefore, rather than define the matrices $\mathbf{A}_\theta$, $\mathbf{B}_\theta$, and $\mathbf{C}_\theta$ for continuous time, the discrete time formulation is given. The Euler method was used for discretising the model. For the AKF it is also necessary to model uncertainty in the model by an additive noise term. By including a Gaussian white noise term with zero mean and known covariance matrix $\mathbf{Q}$, the discrete time augmented state space model is denoted by

$$\boldsymbol{\xi}_\mathrm{t} = \mathbf{A}_\delta\boldsymbol{\xi}_{\mathrm{t}-1} + \mathbf{B}_\delta\boldsymbol{\xi}_{\mathrm{t}-1} \circ \phi\left(\mathbf{C}_\delta\boldsymbol{\xi}_{\mathrm{t}-1}\right) + \mathbf{w}_{\mathrm{t}-1} \tag{20}$$

where $\xi \in R^{N \times 1}$ and the discrete time version matrices $\mathbf{A}_\delta$, $\mathbf{B}_\delta$, $\mathbf{C}_\delta$ are $\in R^{N \times N}$ and have the form

$$\mathbf{A}_\delta = \begin{bmatrix} I + \delta \mathbf{A} & 0 \\ 0 & \mathbf{I}_{n_\theta, n_\theta} \end{bmatrix}, \ \mathbf{B}_\delta = \begin{bmatrix} 0_{n_x, n_x} & \delta \mathbf{B} \\ 0_{n_\theta, n_x} & 0_{n_\theta, n_\theta} \end{bmatrix}, \ \mathbf{C}_\delta = \mathrm{diag}\left(\mathbf{C}, \ 0_{n_\theta, n_\theta}\right) \tag{21}$$

In this study, $N = 13$ is the total number of elements in the augmented state vector, $n_x = 8$ is the number of model states, and $n_\theta = 5$ is the number of model parameters.

In forward models, $\mathbf{w}_{t-1}$ can be used as a driving term to simulate unknown input to the system from afferent connections or from other cortical regions. However, for model inversion purposes, this additional term also facilitates estimation and tracking of parameters via the Kalman filtering. For the Kalman filter, the covariance of $\mathbf{w}_{t-1}$ quantifies the error in the predictions through the model. If one believed the model is accurate, then one would set all the elements of $\mathbf{Q}$ to a small value. On the other hand, a high degree of model-to-brain mismatch can be quantified by setting the elements of $\mathbf{Q}$ to larger values. According to previous works (Karoly et al., 2018; Kuhlmann et al., 2016), a small constant value, $5\mu V$, was used for the model uncertainty, which prevents the filter from converging, and enables new measurements to continue influencing the estimation.

2.5. Model of M/EEG measurements

In general, M/EEG-derived source time-series for each source point can be treated as proportional to the combination of the mean excitatory and inhibitory postsynaptic contributions to the local pyramidal population's mean membrane potential. The measurement model that relates the M/EEG-derived source time-series to the augmented state vector, ξ_t, is given by

$$y_t = \mathbf{H}\xi_t + \mathbf{v}_t \tag{22}$$

where $\mathbf{y}_t$ is the vector of M/EEG source signals at time t, and $\mathbf{v_t} \sim N(0, \mathbf{R})\mathbf{v}_t \sim N(0, \mathbf{R})$ is a zero mean, spatially and temporally independent white Gaussian noise with a standard deviation of 1 mV (Freestone et al., 2014), that simulates measurement errors. The matrix $\mathbf{H}$ when multiplied with the augmented state vector defines a summation of the post-synaptic membrane potentials (corresponding to pyramidal populations) that contribute to each M/EEG source point. Within the context of applying the framework to the canonical NMM, the formulation for each local NMM can be simplified such that $y_t$can be considered a univariate source time-series for each independent NMM and H reduces to a vector. This results in 4714 decoupled NMMs where the local connections are still present and external connections are treated as a lumped input, and 4714 separate estimators. For example, the measurement model of a single NMM (excluding the noise term) is defined as

$$y_t = V_{ip} + V_{ep} + \mu \tag{23}$$

2.6. Analytical Kalman filter

In general, Kalman filters provide the minimum mean squared error estimates for the augmented state vector, under the assumption that they are normally distributed. Assumptions about normality are reasonable if considering the central limit theorem and the population level neurophysiological variables as a mean of the many underlying microscopic neurophysiological variables. As illustrated in Supplementary Fig. 5 the prediction errors of the AKF when applied to real data follow close to a normal distribution, suggesting assumptions about normality are valid. Moreover, without the normality assumption it would be difficult to obtain such an efficient estimation method.

The analytical Kalman filter (AKF) as presented here is a highly stable and accurate iteration on prior works (Freestone et al., 2014; Karoly et al., 2018) that evolved from attempting to follow the same derivation of the original Kalman filter for linear systems, but instead deriving the filter for general nonlinear NMMs using the specific sigmoidal non-linearity given above. Thus, the AKF can be thought of as an assumed density filter. Mathematically stated, the aim of the estimation is to calculate the most likely posterior distribution of the augmented state given the previous measurements,

$$\hat{\xi}_t^+ = E\left[\xi_t | y_1, y_2, \cdots, y_t\right] \tag{24}$$

$$\hat{\mathbf{P}}_t^+ = E\left[\left(\xi_t - \hat{\xi}_t^+\right)\left(\xi_t - \hat{\xi}_t^+\right)^\top\right] \tag{25}$$

which are known as the a posteriori state estimate and its covariance, respectively. In prior work attempting to derive the AKF some of the terms of the state and covariance estimate calculations were difficult to derive analytically and so had to be calculated using the unscented transform as used in the unscented Kalman filter (UKF) for nonlinear systems (Simon, 2006). However, in the current instantiation of the AKF these mathematical difficulties have been overcome and all terms except one are calculated analytically. The remaining term is calculated semi-analytically using the error function. Moreover, the algorithm has been made more numerically stable by including iterative optimisation techniques (Higham, 1988) to ensure the estimated covariance matrix remains positive semi-definite. This leads to a highly stable, accurate and computationally efficient time-domain estimation method.

The estimator proceeds in two stages: prediction and update. In prediction, the prior distribution (obtained from the previous estimate) is propagated through the neural mass equations. This step provides the so called *a priori* estimate, which is a Gaussian distribution with mean and covariance,

$$\hat{\xi}_t^- = E\left[\xi_t | y_1, y_2, \cdots, y_{t-1}\right] \tag{26}$$

$$\hat{\mathbf{P}}_t^- = E\left[\left(\xi_t - \hat{\xi}_t^-\right)\left(\xi_t - \hat{\xi}_t^-\right)^\top\right] \tag{27}$$

In the second stage, the a posteriori state estimate is calculated by correcting the a priori state estimate with measured data by

$$\hat{\xi}_t^+ = \hat{\xi}_t^- + \mathbf{K}_t\left(y_t - \mathbf{H}\hat{\xi}_t^-\right) \tag{28}$$

The weighting to correct the a priori augmented state estimate, $\mathbf{K_t}$, is known as the Kalman gain (Kalman, 1960; Simon, 2006). The Kalman gain is calculated using the available information regarding the confidence in the prediction of the augmented states through the model and the observation model that includes noise by

$$\mathbf{K}_t = \frac{\hat{\mathbf{P}}_t^- \mathbf{H}^\top}{\mathbf{H}\hat{\mathbf{P}}_t^- \mathbf{H}^\top + \mathbf{R}} \tag{29}$$

The a posteriori state estimate covariance is then updated by using the Kalman gain,

$$\hat{\mathbf{P}}_t^+ = \left(\mathbf{I} - \mathbf{K}_t\mathbf{H}\right)\hat{\mathbf{P}}_t^- \tag{30}$$

After each time step, the a posteriori estimate becomes the prior distribution for the next time step, and the filter continues.

The Kalman filter requires $\hat{\xi}_0^+$ and $\hat{\mathbf{P}}_0^+$ to be initialised to provide the a posteriori state estimate and state estimation covariance for time t = 0. We initialised $\hat{\xi}_0^+$ and $\hat{\mathbf{P}}_0^+$ by calculating the mean and covariance of the augmented state vector with the second half of the forward simulation using parameters known to generate alpha rhythms (Freestone et al., 2014; Jansen and Rit, 1995), to obtain a stable model output.

The Appendix further explains how the mean and covariance of the augmented state can be estimated for fully nonlinear NMMs.

2.7. Strong vs weak posterior alpha power-based contrast imaging

It is known that when people are resting, the alpha oscillations at the back of the brain are very strong, especially in the visual cortex and the surrounding occipital region. To study the link between neurophysiological processes and resting-state alpha oscillations, the MEG-derived source recordings were band-pass filtered in the frequency range of 8–12 Hz to extract the alpha power time-series. The alpha band of this group of participants was determined by the dominant alpha frequency of each MEG source point for all participants, and it was found that more than 90% of the MEG source points had an alpha peak frequency in the range of 8–12 Hz. The alpha power envelope measures the amplitude of alpha oscillations and was used as a research target. We calculated the root-mean-square envelope with a sliding window of length $\frac{1}{3}$ second to indicate the temporal evolution of alpha power. In this study, a labelling scheme was defined to identify strong and weak alpha oscillations in the occipital part of the brain. For each subject, the strong and weak occipital alpha power thresholds were determined by the aggregate averaged alpha power of the source points in the occipital lobe. When the posterior alpha power in the occipital lobe exceeds the 75th percentile of the spatially averaged time-series, the relevant time periods were labelled as strong alpha. When the posterior alpha power is less than the 25th percentile of the spatially averaged time-series, the relevant time periods were labelled as weak alpha. Then, the time indices of strong and weak posterior alpha were respectively used to extract the neurophysiological variable estimates. In this way, two sets of neurophysiological variable estimates were obtained for the whole brain MEG source points related to strong and weak posterior alpha oscillation.

For each subject, a two-sample t-test was performed to compare the sample mean of the neurophysiological variable estimates between the strong and weak occipital alpha in each MEG source point. Such that, for every neurophysiological variable, there were 4714 t-statistics to reflect the sample mean differences across the cerebral cortex. Here let X and Y be two random variables, m and n are the sample sizes for X and Y respectively, the two-sample t-statistic is defined as

$$\mathrm{t} = \frac{\overline{X} - \overline{Y}}{\sqrt{\frac{s_X^2}{m} + \frac{s_Y^2}{n}}} \tag{31}$$

where $\overline{X}$ and $\overline{Y}$ are the sample means, s_X^2 and s_Y^2 are the sample standard deviations. In our study, X and Y respectively represented the neurophysiological variable estimates with respect to strong and weak occipital alpha for each source point. The degree of freedom is given by Satterthwaite's approximation and calculated by (Ruxton, 2006; Welch, 1947)

$$\mathrm{df} = \frac{\left(\frac{s_X^2}{m} + \frac{s_Y^2}{n}\right)^2}{\frac{1}{m-1}\left(\frac{s_X^2}{m}\right)^2 + \frac{1}{n-1}\left(\frac{s_Y^2}{n}\right)^2} \tag{32}$$

2.8. Pearson's correlation imaging

Pearson correlation coefficient, $\rho_{X,Y}$, is a measure of linear correlation between two random variables. It is the ratio between the covariance of two random variables and the product of their standard deviations, i.e., for a population, here let X and Y be two random variables:

$$\rho_{X,Y} = \frac{E\left[(X - \mu_X)(Y - \mu_Y)\right]}{\sigma_X \sigma_Y} \tag{33}$$

where μ_X and μ_Y are the mean of X and Y, respectively, and σ_X and σ_Y are the standard deviation of X and Y, respectively.

To measure the linear correlation between the neurophysiological estimate time-series and the alpha power time-series, for each subject sample Pearson's correlation coefficient, r_{XY}, was calculated in each source point. r_{XY} is calculated by

$$r_{XY} = \frac{\sum_{i=1}^{n}\left(X_i - \overline{X}\right)\left(Y_i - \overline{Y}\right)}{\sqrt{\sum_{i=1}^{n}\left(X_i - \overline{X}\right)^2}\sqrt{\sum_{i=1}^{n}\left(Y_i - \overline{Y}\right)^2}} \tag{34}$$

where Y_i is alpha power envelope time-series, $\overline{Y}$ is the mean of the alpha power envelope, X_i is a given neurophysiological variable estimates' time-series, and $\overline{X}$ is the mean of the neurophysiological variable estimates.

2.9. Statistical analysis for group-level brain imaging

The group-level analysis was designed to provide a general pattern of the neurophysiological processes for the resting-state alpha rhythm, which merged statistics from individuals. The brain imaging presented a statistical image: at each voxel, a statistic of interest was computed. The group-level brain imaging showed group-level significant voxels for the statistic of interest. For one type of statistic, every source point had 22 statistic values derived from 22 subjects. To merge statistics from 22 subjects for every source point, a group-level t-statistic was derived by normalising the mean of them by the sample standard deviation. As the brain statistic imaging is a voxel-by-voxel hypothesis testing framework, the multiple comparisons problem ought to be handled. We used established nonparametric and (statistical) parametric mapping (SPM) to account for the multiple comparison problem over sources (Nichols and Holmes, 2002), after interpolating point source data into images. Nonparametric procedures use the null distribution of the maximum statistic over sources (i.e., voxels), while standard SPM analyses use analytic results from random field theory. In this paper, we report nonparametric statistical maps, but confirmed their consistency with standard statistical parametric maps (Friston et al., 1994; Worsley et al., 1992, 1996). We used two kinds of statistical parametric mapping. The first statistical parameter was based upon t-statistics testing parameter estimates differences between conditions; namely, strong and weak posterior alpha power. These analyses were used to test for systematic differences in the time averages of various parameter estimates, such as the extrinsic input μ. To complement these characterizations — of the neuronal correlates of high and low alpha — we used Pearson's correlation coefficient to test for correlations between timeseries of estimated neuronal dynamics and the expression of alpha power over time. In short, we asked whether the estimates of neuronal activity based upon our filtering scheme could predict differences in the expression of alpha power; either in terms of categorical, condition-specific differences (using contrasts of averages over time) or in terms of correlations over time.

With MATLAB package Fieldtrip and customized scripts, the brain imaging was generated by projecting significant group-level t-statistics (after corrections for multiple comparisons) to the corresponding cerebrocortical source points on the template MRI. The imaging was further rendered by linearly interpolating the value of each source point to the surrounding cerebrocortical voxels (Oostenveld et al., 2011). Consequently, the group-level brain imaging showed the statistically significant brain areas of the AAL Atlas with respect to the statistic of interest.

3. Results

3.1. Individual example of brain imaging of resting-state neural processes

To illustrate the approach for one individual, Fig. 1b shows a sample MEG source time-series from an occipital cortical source (MNI-coordinates: 12, −90, 24) derived by the LCMV beamformer (Van Veen et al., 1997). The figure focuses on occipital cortex because it is known

to be a strong generator of resting-state alpha rhythm. Fig. 1c shows the extracted alpha oscillation in red and its power envelope in green. Fig. 1d-k illustrates the corresponding estimates of the neurophysiological variables of the NMM, obtained by the AKF. The estimates of the variables converge after a short time and are relatively stable during the resting-state. Moreover, the time-resolved variable estimates afford the possibility to analyse their relationship with other target variables whether they are endogenous or exogeneous in nature. Here for simplicity their relationship with the intermittent waxing and waning of alpha rhythm power (root-mean-square envelope) during resting was considered. This was analysed further at the group level in the following subsections, however, as a first step Fig. 1l displays example brain contrast imaging results for the same individual in Fig. 1b-k where the neurophysiological variable estimates of each source point obtained during strong and weak occipital alpha are contrasted using a two-sample *t*-test (significance level $\alpha = 0.05$). Only significant voxels were activated after multiple comparisons correction for the whole brain. Note only the neurophysiological variable sub-images should be interpreted with respect to statistical testing, not the alpha power sub-image on the left because the null hypothesis is that a given variable is equal during both strong and weak alpha power periods. Application of the t-statistic to the alpha power sub-image was done purely as a standardised way to view the data. It can be seen that increases in the external cortical input, μ, is a strong determinant of increased posterior alpha power, while the other neurophysiological variables also appear to contribute. It is also important to note that the NMM only approximates population activity in the cerebral cortex. Therefore, associated variable estimates should be considered approximations of true neurophysiological changes.

A comparison (Supplementary Fig. 1–4) shows the superiority, in this context, of the AKF over the most common Kalman filtering scheme for nonlinear systems, unscented Kalman filtering (UKF). Briefly, the results indicated that the AKF is 7.5 times faster than the UKF in processing 3.75-minutes of data, 10% more accurate in tracking model variables, and only took half time that UKF did in finding the ground-truth. For tracking the actual measurement, AKF showed excellent accuracy in both time and frequency domain (Supplementary Fig. 5 and 6).

3.2. Group-level brain imaging of resting-state neural processes

The same individual analysis presented in Fig. 1 was applied to MEG resting-state data from 22 subjects and a group analysis was subsequently performed. Along with traditional contrast-based imaging (Penny et al., 2011), this study provides correlation-based imaging as an alternative type of visualization that leverages the space-time resolved nature of the neurophysiological variable estimates to illustrate the neural processes in modulating alpha power. For each type of imaging and each source point, statistics were derived first at the individual level, and finally merged into the group-level. The multiple comparisons problem was handled by a nonparametric permutation approach (Nichols and Holmes, 2002). The six most significant brain structures associated with each neurophysiological variable were noted in Supplementary Table 2 and are discussed further below. The max t-statistic and the voxel's coordinate were also presented.

3.2.1. Contrast imaging

Fig. 2 shows the group-level contrast imaging of the mean difference of alpha power and neurophysiological variable estimates between strong and weak occipital alpha power. As with Fig. 1l, only the neurophysiological variable sub-images should be interpreted with respect to statistical testing.

In Fig. 2a, the brain exhibited strong bilateral posterior alpha oscillations. The alpha oscillation in the occipital lobe was the most noticeable, whereas the parietal and temporal lobes had weaker alpha oscillations. Bilateral cingulate gyrus also showed a clear alpha rhythm. The medial cerebral cortex showed more potent alpha oscillations than the lateral. Across the whole brain, four hotspots can be identified from Fig. 2a: right cuneus (MNI-coordinates: 12, −90, 24, group-level t-statistic≈30), right calcarine fissure (MNI-coordinates: 12, −96, −6, group-level t-statistic≈29), right anterior cingulate gyrus (MNI-coordinates: 6, 36, 12, group-level t-statistic≈27) and right precuneus (MNI-coordinates: 6, −48, 18, group-level t-statistic≈26). The localised relationship between alpha power and each neurophysiological variable estimate for the identified brain regions is illustrated in Supplementary Fig. 7. Fig. 2b shows that strong occipital alpha power was primarily related to large external input, μ, in the bilateral occipital and temporal lobes and particularly in the right middle temporal gyrus, bilateral calcarine fissure and surrounding cortex, and bilateral lingual gyrus. In Fig. 2c, occipital alpha power change was strongly related to the mean inhibitory interneuron membrane potential, V_i, in the left lingual gyrus, bilateral precuneus, left cuneus, and bilateral calcarine fissure and surrounding cortex, where high V_i caused strong occipital alpha power. Fig. 2d shows only a few illuminated voxels in the occipital and temporal lobes, implying that the occipital alpha power change has a trivial relationship with the excitatory interneurons. In Fig. 2e, the pyramidal membrane potential, V_p, at the back of the head dropped when the occipital alpha power was strong and especially in the right lingual gyrus, fusiform gyrus, inferior occipital gyrus, calcarine fissure and surrounding cortex, and inferior and middle temporal gyri.

3.2.2. Pearson's correlation imaging

Pearson's correlation imaging in Fig. 3 shows the brain areas with significant group-level linear correlation between each neurophysiological variable and local, rather than posterior, alpha power.

In Fig. 3a, the mean excitatory to pyramidal connection strength, α_{ep}, was linearly related to alpha power in bilateral frontal lobes, and especially in the right medial orbital part of superior frontal gyrus, bilateral gyrus rectus, left olfactory cortex, and left orbital part of superior frontal gyrus. In Fig. 3b, the external input, μ, was correlated with alpha power in bilateral occipital and frontal lobes. Particularly, positive correlation was observed in bilateral calcarine fissure and surrounding cortex, and left lingual gyrus, while negative correlation was observed in the left gyrus rectus and left orbital part of superior frontal gyrus. Fig. 3c shows that the alpha power exhibited positive correlation with the mean membrane potential of inhibitory interneurons, V_i, in bilateral occipital and temporal lobes. Left lingual gyrus, left inferior occipital gyrus, left calcarine fissure and surrounding cortex, left cuneus, and bilateral inferior temporal gyrus were identified as the most prominent brain structures. Fig. 3d indicates that the mean membrane potential of excitatory interneurons, V_e, had substantial positive correlation with alpha power in bilateral frontal lobes such as left orbital part of inferior frontal gyrus, right medial orbital part of superior frontal gyrus, bilateral gyrus rectus. V_e in the right inferior temporal gyrus and insula cortex also showed significant positive correlation with alpha power. Fig. 3e reveals that alpha power increased with the decrease of the mean membrane potential of pyramidal cells, V_p, in bilateral lingual gyrus, and bilateral calcarine fissure and surrounding cortex. On the contrary, V_p was positively correlated with alpha power in the frontal lobe such as right medial orbital part of superior frontal gyrus, and right orbital part of inferior frontal gyrus.

3.3. Relationship between resting-state networks and alpha-power-linked neurophysiology

Table 1 summarises which of the previously well studied resting-state sub-network (Beckmann et al., 2005; Brookes et al., 2011; Farras-Permanyer et al., 2019; Hipp et al., 2012) nodes contained statistically significant alpha-power-linked neurophysiological variable changes for both contrast and correlation imaging. Consistent results are observed for both imaging methods with primarily external input, but also the mean membrane potential variables, having significant and varied influence on alpha power within resting-state sub-network nodes.

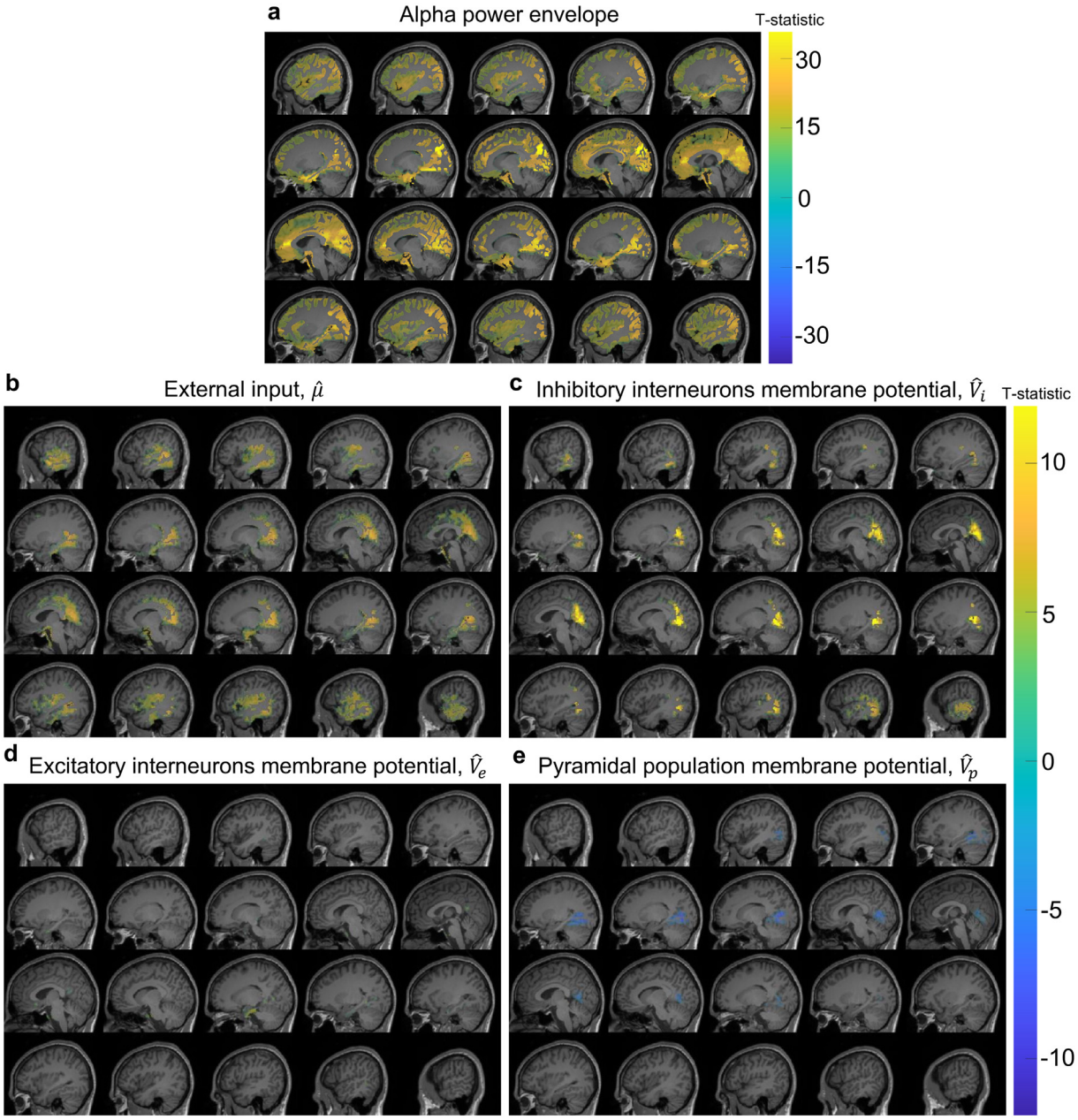

Fig. 2. Group-level contrast imaging. It shows the mean difference of alpha power (rms envelope) and neurophysiological variable estimates between two conditions: occipital strong and weak alpha oscillations. The activated areas in the sub-images represents statistically significant difference was observed after corrections for multiple comparisons (significance level $\alpha = 0.05$). (a) Contrast imaging of alpha power. (b) – (e) Contrast imaging of external cortical input, the mean inhibitory interneuron membrane potential, the mean excitatory interneuron membrane potential, and the mean pyramidal membrane potential. Only neurophysiological variables that showed statistically significant changes after correction for multiple comparisons are displayed.

4. Discussion

Here a NMM inference-based brain imaging framework has been proposed as a general method to provide reliable spatial and temporal information about the latent neural processes of complex brain states.

4.1. A novel way to image neural processes across the brain

To quote the famous statistician George Box, this paper takes the perspective that “all models are wrong, but some are useful”. Although the canonical NMM applied here is designed primarily to model alpha rhythms and visual evoked responses (Jansen and Rit, 1995), the mathematical framework presented here is general enough to allow researchers to implement arbitrary NMMs that are more relevant and useful for their study of interest. At the same time, many fMRI mapping studies have relied on a canonical HRF (Aquino et al., 2014; Handwerker et al., 2004), therefore neurophysiological variable mapping studies of the kind presented here that depend on a canonical NMM should also be useful for both imaging and understanding brain function in different ways (Schiff, 2012), despite the obvious approximations of the canonical model. Using more complex and accurate models makes the inference problem more difficult and requires more measurements of brain signals to reduce the non-uniqueness of the solution space and find a more optimal solution. Therefore, the current best path forward is to trade off physiological detail for speed and accurate solutions to achieve results that are useful and interpretable. This is important in

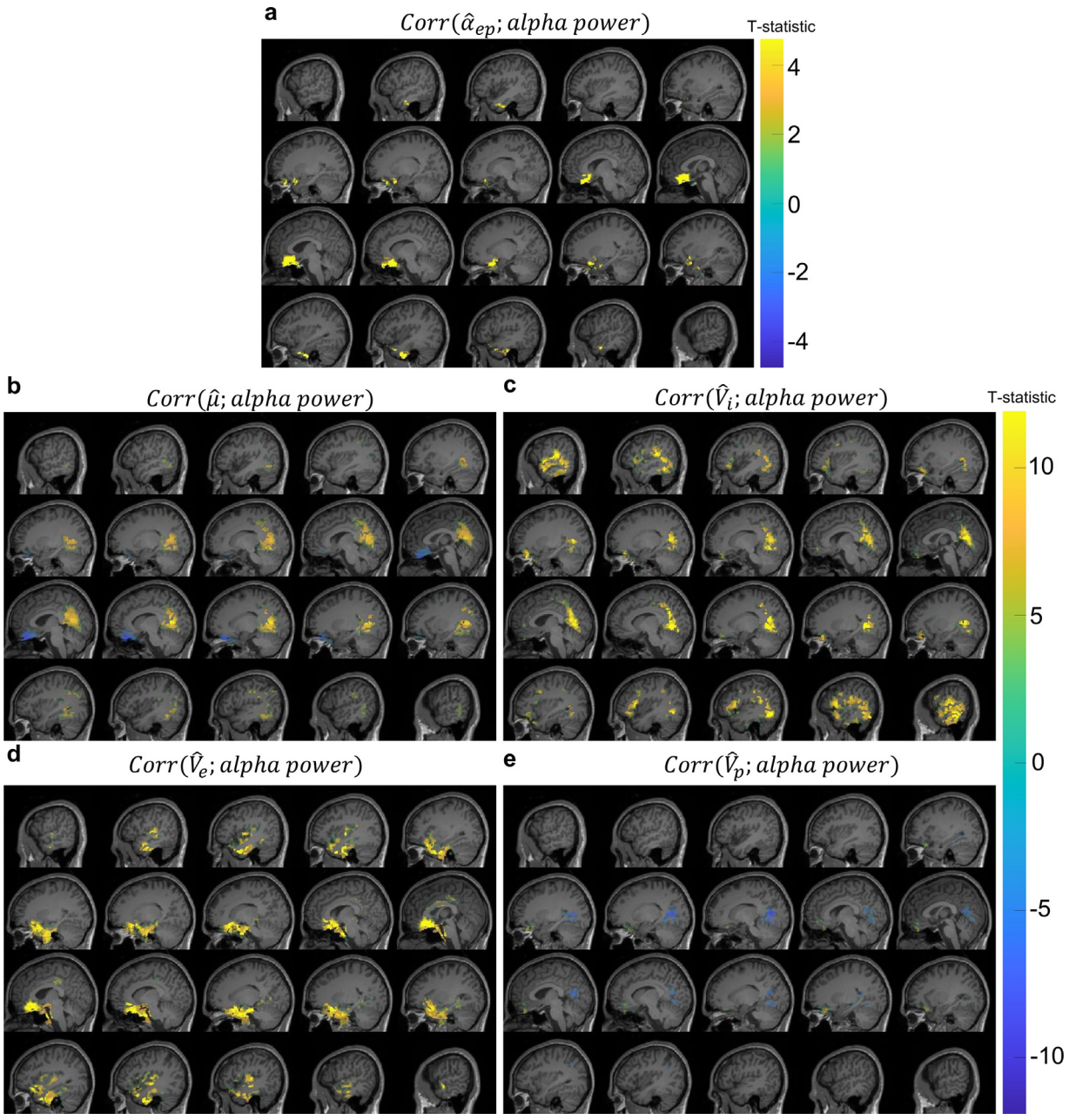

Fig. 3. Group-level correlation coefficient imaging. It reveals brain regions where a significant linear correlation between neurophysiological variable estimates and alpha power was observed. The activated areas in the sub-images represents statistically significant correlation was observed after corrections for multiple comparisons (significance level $\alpha = 0.05$). (a) – (e) Correlation imaging between alpha power and the excitatory to pyramidal connection strength, external cortical input, the mean inhibitory interneuron membrane potential, the mean excitatory interneuron membrane potential, and the mean pyramidal membrane potential. Only neurophysiological variables that showed statistically significant changes after correction for multiple comparisons are displayed.

human neuroscience as invasive experimental methods typically used to achieve neurophysiological insights are often difficult to apply.

Here the neurophysiological estimates have been visualised with contrast imaging and correlation imaging, which associate the neurophysiological variables with a target time-series, alpha-power envelope. However, in general the target could be a behavioural responsiveness variable, exogenous stimulus, or cognitive measure. This suggests broad applicability of the framework. Estimating neurophysiological variables in a time-resolved fashion also opens the door for detecting, and controlling, local critical transitions (Breakspear, 2017) across the brain to study different brain states, such as waking, sleeping, intra-awake or other states.

4.2. Neural processes that modulate the alpha power

As an example, the framework was applied to resting-state alpha rhythm data to provide new insights. The neural processes underlying the alpha rhythm are still uncertain with debate around the source of the alpha rhythm being the thalamus, thalamocortical loops, the cortex and/or intracortical inhibition (Freyer et al., 2011; Halgren et al., 2019; Liley et al., 2001; Lozano-Soldevilla, 2018). Given the complexity of the brain it is likely that alpha rhythms can emerge in different ways depending on axonal and dendritic propagation delays between interacting brain networks or the time constants of excitatory or inhibitory synaptic potentials in these brain networks. Recent human electrophysiology

Table 1
Resting-state sub-networks, their AAL atlas ROIs, and the corresponding maximum group-level t-statistic for statistically significant neurophysiological variables for contrast and correlation imaging. Five resting-state networks are included, namely Default Mode Network (DMN), anterior Default Mode Network (DMNa), ventral Default Mode Network (DMNv), Sensorimotor resting state network (SM), and Visual resting state network (Visual). This table shows if the areas listed in these resting state networks have significant changes in the physiological variables by showing the group-level t-statistic if they are significant, otherwise leaving the space unmarked. Only neurophysiological variables having significant t-statistic source points are presented.

	Region name	Contrast imaging				Correlation imaging				
		μ	V_i	V_e	V_p	α_{ep}	μ	V_i	V_e	V_p
DMN	Parietal_Sup_L	5.52	5.90				5.52			
	Parietal_Sup_R						5.22			
	Parietal_Inf_L	5.72	6.43				5.98	8.94		
	Parietal_Inf_R						5.16			
	Temporal_Mid_L	8.66	10.29	5.59			7.86	12.20	11.99	
	Temporal_Mid_R	10.12	8.57		−6.43		5.81	11.98	12.91	
DMNa	Insula_L	7.72				6.87		7.42	10.00	
	Insula_R	8.06	7.15					8.99	15.04	
	Cingulum_Ant_L	6.15						5.87	8.90	
	Cingulum_Ant_R	5.62						5.56	9.23	
	Temporal_Pole_Mid_L					5.78		8.33	10.20	
	Temporal_Pole_Mid_R	5.31	5.43					5.54	11.52	
DMNv	Cingulum_Post_L	8.02	9.83				8.05	8.29		
	Cingulum_Post_R	7.90	10.33				7.16	7.84	6.43	
	Hippocampus_L									
	Hippocampus_R									
	ParaHippocampal_L	7.43		6.74	−5.48	5.92	8.28		12.15	−5.61
	ParaHippocampal_R	7.84			−5.91	6.06			10.93	
	Fusiform_L	7.99	11.69	5.81		5.61	7.02	9.72	10.93	
	Fusiform_R	7.83	8.92	6.73	−7.52		6.87	9.08	13.06	−5.98
	Angular_L	5.72	9.66				5.95	6.14		−5.96
	Angular_R	5.82	9.42				5.69	9.19		
	Precuneus_L	8.69	16.04	6.64	−5.93		7.81	11.56		−5.59
	Precuneus_R	8.45	14.37				7.85	11.52	8.25	
SM	Precentral_L	6.05					5.32	7.29	6.10	
	Precentral_R	5.56						6.29		
	Frontal_Mid_L	4.93						8.04		
	Frontal_Mid_R	5.64						8.11		
	Supp_Motor_Area_L	6.17						6.05		
	Supp_Motor_Area_R	5.61	5.43							
	Postcentral_L	9.13	5.41		−5.47		6.09	7.24		
	Postcentral_R	6.17					5.58	7.06		
	SupraMarginal_L	7.01	6.87				6.92	9.29		
	SupraMarginal_R	6.93	8.05				5.82	8.65		
	Paracentral_Lobule_L	6.11	6.31				5.64	7.82		
	Paracentral_Lobule_R	5.55	6.19				6.67			
Visual	Calcarine_L	9.69	14.17		−6.01		10.49	14.12		−6.90
	Calcarine_R	9.31	13.33		−7.20		9.09	11.36		−7.99
	Cuneus_L	8.26	13.52		−5.64		7.86	14.08		−5.43
	Cuneus_R	7.69	8.88				6.44	7.26		
	Lingual_L	9.34	18.80	7.75	−5.99		8.36	16.65	10.26	−7.80
	Lingual_R	9.54	11.53	6.04	−9.04		8.11	11.11	10.34	−8.24
	Occipital_Sup_L	7.20	7.23				6.14	5.92		
	Occipital_Sup_R						5.07			−5.34
	Occipital_Mid_L	5.99	8.92				7.59	6.55		
	Occipital_Mid_R				−6.17					

research regarding phase relationships of the alpha rhythm has shown that higher-order posterior cerebral cortex leads lower-order posterior cortex, posterior cortex leads the pulvinar nucleus of the thalamus, and the alpha rhythm is predominantly present in the superficial layers (I/II) of cortex (Halgren et al., 2019). This suggests a role for the alpha rhythm in top-down feedback processing. While the results presented here for the contrast and correlation imaging, do not focus on which brain areas lead each other, they instead identify the local relationship between alpha rhythm power and population averaged membrane potentials of the pyramidal, excitatory, and inhibitory populations and their population averaged excitatory and inhibitory synaptic connection strengths. This helps to determine which neurophysiological variables are critical contributors to the alpha rhythm across the entire human brain. While phase-lag relationships between the estimated variables could be determined, it is considered beyond the scope of the current paper, and now that the most critical brain areas have been identified in this study, it opens the door for a more focused study that could apply the framework presented here to determine the long-range connection strengths between these critical areas to better determine which areas drive each other. By using the current framework to help narrow down the critical brain areas, it makes the problem of estimating the long-range connection strengths more tractable as it reduces the complexity of the model and the solution space by considering only the critical areas instead of the whole brain.

Regarding the prior observation that alpha rhythm is dominant in the superficial layers of posterior cerebral cortex (Halgren et al., 2019), the canonical model presented here only includes three neural populations in order to make the inference problem more accurate by keeping it simpler. These pyramidal, excitatory, and inhibitory populations have previously been attributed to the internal pyramidal (V), internal granular (IV), and external granular (II) layers (Freestone et al., 2014). Consistent with this assignment, the contrast and correlation imaging in Figs. 2 and 3 both revealed that the average membrane potential of the inhibitory interneuron population had a strong positive relation-

ship with alpha power in posterior cortex. This suggests a potential link between the alpha power observed electrophysiologically in superficial layers of posterior cortex and inhibition, however, further work would be needed to study this more accurately using a NMM that considers greater laminar cortical detail.

Regarding the brain areas and networks involved in the resting state and the alpha rhythm, many studies using fMRI and electromagnetic source imaging have identified different resting-state networks (Beckmann et al., 2005; Brookes et al., 2011; Hipp et al., 2012). With respect to MEG, default mode, somatosensory, visual, and other resting-state networks have been identified with significant hubs tied to frequencies close to alpha in lateral parietal cortex, medial and dorsal prefrontal cortex, and temporal cortex (Brookes et al., 2011; Hipp et al., 2012). The contrast and correlation imaging results presented here confirm there are significant changes in the neurophysiological variables, μ and V_i predominantly within the previously identified resting-state networks (Brookes et al., 2011; Farras-Permanyer et al., 2019; Hipp et al., 2012), as shown in Table 1. Particularly, μ, representing the external cortical input, was critical in resting-state networks showing significant group-level t-statistic in both imaging types. Another interesting observation in the correlation imaging relates to μ, which can be regarded as a linear combination of all inputs from all other areas and within the context of dynamical systems theory is known to be a critical bifurcation parameter in the canonical NMM. Within the range of the estimated values of μ, prior mathematical bifurcation analysis of this model showed a u-shaped pattern for alpha power in the model output with escalating μ: as μ increases, moderate amplitude alpha-like activity emerges in the model, followed by approximately 3 Hz spike-like activity where alpha band content weakens, and finally the model transitions to strong alpha oscillations (Grimbert and Faugeras, 2006). Fig. 3b demonstrates that μ was negatively correlated with alpha power in the medial orbital part of superior frontal gyrus, gyrus rectus and olfactory cortex, and positively correlated with alpha power in the anterior part of occipital lobe. The bifurcation analysis can help explain the inconsistent correlations in frontal and occipital lobes: frontal source points (Supplementary Fig. 8a-e) and occipital source points (Supplementary Fig. 8f-j) correspond to the left and right sides of the u-shaped relationship between μ and alpha power, respectively. Considering μ as the inter-regional communication, the result here corroborates earlier EEG-fMRI studies that negative correlation was observed between blood-oxygen-level-dependant functional connectivity and alpha power in the extensive areas of the frontal lobe, while positive correlation was observed in the vicinity of thalamus (Gonçalves et al., 2006; Tagliazucchi et al., 2012). More research is needed to investigate the physiological meaning of these correlations.

4.3. Rationality and novelty of the framework

4.3.1. Selection of model

The Jansen-Rit (JR) neural mass model (Jansen and Rit, 1995) is the canonical model used in the framework. The choice of this model is consistent with the idea of Occam's razor, that is, one should start with the model with the fewest assumptions that is still able to describe the data. Although many neural models have been specifically designed to describe different brain states in more detail, the model we used is physiologically informative, compatible with M/EEG, and efficient enough for whole brain modelling. Another aspect of the framework is decoupling of the NMMs. This means there are no long-range connections between the NMMs and instead a lumped external cortical input is locally estimated. This design allows whole brain modelling, and each model fits an MEG source point, 4714 in total, which results in fine-grained neuroimaging with a resolution of 6 mm source spacing. The inference problem for interconnected NMMs would involve estimation of a 4714×4714 connection strength matrix and would therefore involve a more complex solution space and require much more computation. Additional constraints are needed to simplify the problem such as using diffusion tensor imaging based tractography (Mukherjee et al., 2008) to determine which of the connections should exist, or as noted above once critical brain areas and their neurophysiological changes are identified through the proposed framework, the interconnection of these critical nodes can be investigated in a more tractable study. Although interconnected NMM networks may provide more information (e.g., how an epileptic seizure may spread from a subnetwork in a brain region (Hashemi et al., 2021)), there are still studies employing uncoupled modelling and showing local dynamics can disclose the underlying neural processes to some degree (Ritter et al., 2013). All in all, this is a trade-off between how much time and resources one has and how general and applicable the framework is.

4.3.2. Innovation of the model inversion scheme

The NMM is a nonlinear dynamical system that maps neurophysiological variables to electromagnetic brain activity. Model inversion techniques estimate unobserved neurophysiological variables from the actual measurement. Model inversion schemes can be divided into frequency-domain and time-domain methods. Frequency-domain methods estimate parameters normally based on the power spectrum in which the analytical power spectrum is derived from the model and optimisation methods are used to minimise the objective function constructed with the model's spectrum and the observed spectrum (Hashemi et al., 2018). The optimisation methods comprise gradient-based (e.g., Levenberg-Marquardt and Gauss-Newton) and black box optimisation algorithms (e.g., particle swarm optimisation and Genetic algorithm). Black box optimisation algorithms are usually more powerful in finding the global minimum than gradient-based methods, although they usually require much more time and memory (Cuevas et al., 2014; Georgieva and Jordanov, 2009). Time-domain methods, like the Kalman filter, iteratively estimate the posterior distribution of the parameters when a new measurement comes in. In summary, frequency-domain estimation methods provide parameter estimates reflecting the general neuronal dynamics underlying the whole measurement, whereas time-domain methods provide the temporal evolution of the parameter estimates. As the present framework aims to show the temporal pattern of the parameter estimates under some brain conditions (for example Fig. 3 temporal correlation imaging), time-domain methods (e.g., the Kalman filter) are more appropriate.

In existing studies, Bayesian inference principally relies on simplifying assumptions, sampling methods, or re-framing the problem for nonlinear systems (Daunizeau et al., 2011; Friston et al., 2003; Simon, 2006). The extended Kalman filter works on the principle that a linearized transformation of means and covariances of variables of interest are approximately equal to the true nonlinear transformation. Nonetheless, it has been shown in certain situations that the approximation is not satisfactory and leads to non-optimal estimation (Simon, 2006). The unscented Kalman filter (UKF) is time-consuming because it reconstructs the mean and covariance by propagating sampled sigma points (Simon, 2006), and is therefore less efficient at estimating variables for thousands of models. The variational Bayes used by DCM iteratively converges to the actual variables, but it is a relatively computationally intensive frequency domain method that cannot effectively provide the evolution of the variables with high time resolution (David et al., 2006; Friston, 2002; Prando et al., 2020; Van de Steen et al., 2019). Alternatively, the AKF used in our framework involves a fast, semi-analytic solution to propagate means and covariance of the neurophysiological variables of the fully nonlinear NMM. As indicated in the results the AKF is much more efficient and accurate than the UKF.

In terms of related work, several approaches have been proposed for estimating effective connectivity, implicitly synaptic parameters, from large numbers of nodes in distributed neuronal networks. Perhaps the most notable is a simplification of DCM using an autoregressive formulation (Frässle et al., 2017). Effectively, this linearizes a simple neural mass model for fMRI timeseries and, crucially, enables the estimation or inversion to proceed on a node-by-node basis. However, this technology has only been applied to very simple models for fMRI timeseries and

cannot accommodate the expressive neural mass models entertained in the current paper. Technically, one could view the current procedure as a stochastic DCM. Stochastic DCM has been developed for fMRI time-series using simple (bilinear) approximations to a neural mass model. When using generalised (Bayesian or variational) filtering, stochastic DCM uses the same design described above; namely, augmenting the state space with a parameter space - so that the parameters are estimated as slowly fluctuating states (Li et al., 2011). Both our approach and stochastic DCM can be regarded as variations of Kalman filters that handle the estimation of noise and conditional covariance components in a graceful (Bayes optimal) fashion. However, stochastic DCM has not been applied to expressive neural mass models of the kind required for EEG and MEG.

4.3.3. Framework versatility and modularity

This framework can image neural activity for a wide range of brain oscillations, from delta (1–4 Hz) to gamma (>30 Hz), because the NMM can generate stable output in these frequencies (David and Friston, 2003). Moreover, the NMM used in this framework has also been employed in studying the alpha rhythm, epileptiform activity, and anaesthesia in previous works (Hartoyo et al., 2019; Karoly et al., 2018; Kuhlmann et al., 2016). Therefore, neurophysiological estimates can be used to understand the neural processes behind these brain states. Modularity is another feature of the framework, in which each module is independent and replaceable, i.e., the NMM or even the inference method can be replaced. This approach was taken to enable release of the framework as a software called NeuroProcImager (see Code Availability) so that prior M/EEG source imaging studies could be extended by inputting the source time-series in MNI template coordinates and obtaining neurophysiological variable time-series. This modular approach to the framework for nonlinear neural systems is different from prior end-to-end source imaging work involving only the linear Kalman filter and autoregressive models (also only linear and not neural) which sought to derive brain current sources directly from electromagnetic sensor measurements (Galka et al., 2004; Lamus et al., 2012). The modularity, versatility, efficiency, and accuracy of the framework suggests it will have broad applicability to inferring neural processes underlying different brain states.

4.3.4. Limitations and future perpectives

One of the key applications of dynamic causal modelling is to test hypotheses about different functional architectures (David et al., 2006; Friston et al., 2003, 2019; Kiebel et al., 2008; Van de Steen et al., 2019), e.g., whether a particular condition or drug effect is expressed on one synaptic parameter or another. This rests upon being able to assess the marginal likelihood or Bayesian model evidence of different models. In future work, we will address the evaluation of model evidence under our semi-analytical Kalman filtering scheme and illustrate the application of Bayesian model comparison, when testing hypotheses about neuronal processing and computation in health and disease.

Author contribution

All authors wrote the paper. Experiment planning and data collection involved A.P., S.M., W.W., D.L. and L.K. Development of the inference-based imaging framework and its application involved Y.Z, M.B., P.J.K., D.R.F., Y. L., D.L. and L.K.

Declaration of Competing Interests

The authors declare they have no competing financial interests.

Credit authorship contribution statement

Yun Zhao: Conceptualization, Methodology, Software, Validation, Formal analysis, Writing – original draft, Writing – review & editing, Visualization. **Mario Boley:** Conceptualization, Methodology, Writing – original draft, Writing – review & editing. **Andria Pelentritou:** Resources, Data curation, Writing – original draft, Writing – review & editing. **Philippa J. Karoly:** Methodology, Software, Writing – original draft, Writing – review & editing. **Dean R. Freestone:** Methodology, Software, Writing – original draft, Writing – review & editing. **Yueyang Liu:** Software, Writing – original draft, Writing – review & editing. **Suresh Muthukumaraswamy:** Resources, Data curation, Writing – original draft, Writing – review & editing. **William Woods:** Resources, Data curation, Writing – original draft, Writing – review & editing. **David Liley:** Conceptualization, Resources, Data curation, Writing – original draft, Writing – review & editing, Funding acquisition. **Levin Kuhlmann:** Conceptualization, Methodology, Resources, Data curation, Supervision, Writing – original draft, Writing – review & editing, Project administration, Funding acquisition.

Data and code availability

The 22 healthy male resting-state MEG data and their corresponding MRI data are available at http://consciouscloud.erc.monash.edu. The inference-based neural processes imaging framework is implemented in a MATLAB package called NeuroProcImager and is available at https://github.com/yundumbledore/NeuroProcImager. A demonstration of the package is provided in the Supplementary Information and the Github repository along with instructions on how to apply the framework to the provided demonstration data or other pre-existing source imaging data.

Acknowledgements

We thank Naotsugu Tsuchiya and David Grayden for helpful preliminary discussions about the work, along with MASSIVE (https://www.massive.org.au) for computational resources. This work was supported by a grant from the Australian Research Council (DP200102600) and Monash University.

Supplementary materials

Supplementary material associated with this article can be found, in the online version, at doi:10.1016/j.neuroimage.2022.119592.

Appendix

This appendix is for mathematical derivation of the analytical Kalman filter. As noted above, in general the Kalman filter does not have a solution for nonlinear models. Previous works that used Kalman filtering on the nonlinear NMMs have relied on simplifying assumptions (either linearization of the model, or sampling to estimate the posterior distribution) (Escuain-Poole et al., 2018; Hartoyo et al., 2019; Liu and Gao, 2013). This work applied an exact, semi-analytic solution for the mean and covariance of a multivariate Gaussian distribution transformed by the nonlinear NMM. For simplicity of expression, the term $\mathbf{B}_\delta\xi_{t-1}\circ\phi(\mathbf{C}_\delta\xi_{t-1})$ can be written as $\phi(\xi_{t-1})$. This solution provides the a priori estimate of the mean,

$$\begin{aligned}\hat{\xi}_t^- &= E\left[\xi_t|y_1, y_2, \cdots, y_{t-1}\right]\\ &= E\left[\mathbf{A}_\delta\xi_{t-1} + \mathbf{B}_\delta\xi_{t-1}\circ\phi\left(\mathbf{C}_\delta\xi_{t-1}\right) + \mathbf{w}_{t-1}\right]\\ &= \mathbf{A}_\delta\hat{\xi}_{t-1}^+ + E\left[\phi\left(\xi_{t-1}\right)\right].\end{aligned} \tag{A1}$$

This solution provides the a priori estimate of the covariance,

$$\begin{aligned}\hat{\mathbf{P}}_t^- &= E\left[\left(\xi_t - \hat{\xi}_t^-\right)\left(\xi_t - \hat{\xi}_t^-\right)^\top\right]\\ &= E\left[\left(\mathbf{A}_\delta\xi_{t-1} + \phi\left(\xi_{t-1}\right) + \mathbf{w}_{t-1} - \mathbf{A}_\delta\hat{\xi}_{t-1}^+ - E\left[\phi\left(\xi_{t-1}\right)\right]\right)(\cdot)^\top\right]\\ &= E\left[\mathbf{A}_\delta\left(\left(\xi_{t-1} - \hat{\xi}_{t-1}^+\right) + \phi\left(\xi_{t-1}\right) + \mathbf{w}_{t-1} - E\left[\phi\left(\xi_{t-1}\right)\right]\right)(\cdot)^\top\right]\end{aligned} \tag{A2}$$

For notational convenience, we denoted the vectors inside the brackets in order as $a = \mathbf{A}_\delta(\xi_{t-1} - \hat{\xi}^+_{t-1})$, $b = \phi(\xi_{t-1})$, $c = \mathbf{w}_{t-1}$, $d = E[\phi(\xi_{t-1})]$, which gives

$$\hat{\mathbf{P}}^-_t = E\left[(a+b+c-d)(\cdot)^\top\right] \tag{A3}$$

It is given that

$$\begin{aligned}
&E[c] = 0\\
&E\left[ca^\top\right] = E\left[cb^\top\right] = E\left[cd^\top\right] = 0\\
&E\left[cc^\top\right] = \mathbf{Q}\\
&E\left[aa^\top\right] = \mathbf{A}_\delta \hat{\mathbf{P}}^+_{t-1}\mathbf{A}^\top_\delta\\
&E\left[dd^\top\right] = dd^\top\\
&E[a] = 0\\
&E[b] = d.
\end{aligned} \tag{A4}$$

Using the identities to simplify the expression for $\hat{\mathbf{P}}^-_t$ and substituting back in, $\hat{\mathbf{P}}^-_t$ is calculated by

$$\begin{aligned}
\hat{\mathbf{P}}^-_t = {} & \mathbf{A}_\delta \hat{\mathbf{P}}^+_{t-1}\mathbf{A}^T_\delta + \boldsymbol{Q} - E\left[\phi(\xi_{t-1})\right]E\left[\phi(\xi_{t-1})^\top\right] - \mathbf{A}_\delta \hat{\xi}^+_{t-1}E\left[\phi(\xi_{t-1})^\top\right]\\
& - E\left[\phi(\xi_{t-1})\right]\left(\mathbf{A}_\delta \hat{\xi}^+_{t-1}\right)^\top + E\left[\phi(\xi_{t-1})\phi(\xi_{t-1})^\top\right]\\
& + E\left[\left((\mathbf{A}_\delta \xi_{t-1})\phi^\top(\xi_{t-1})\right] + E\left[\phi(\xi_{t-1})(\mathbf{A}_\delta \xi_{t-1})^\top\right]
\end{aligned} \tag{A5}$$

The expectation terms that can be analytically derived are $E[\phi(\xi_{t-1})]$, $E[(\mathbf{A}_\delta\xi_{t-1})\phi^\top(\xi_{t-1})]$, and $E[\phi(\xi_{t-1})(\mathbf{A}_\delta\xi_{t-1})^\top]$ where $E[(\mathbf{A}_\delta\xi_{t-1})\phi^\top(\xi_{t-1})] = E[\phi(\xi_{t-1})(\mathbf{A}_\delta\xi_{t-1})^\top]^\top$. Thus, the analytical solution for $E[\phi(\xi_{t-1})]$ and $E[\phi(\xi_{t-1})(\mathbf{A}_\delta\xi_{t-1})^\top]$ are derived. A semi-analytical solution is provided for $E[\phi(\xi_{t-1})\phi(\xi_{t-1})^\top]$.

For the ease of understanding the following derivations of the above terms, the constant linear terms $\mathbf{A}_\delta$, $\mathbf{B}_\delta$, $\mathbf{C}_\delta$ have been set equivalent to identity matrices of the appropriate dimension. However, in the MATLAB code we used the true matrices and full derivation. Notably, symbols $\boldsymbol{x}$, μ below should not be confused with $\mathbf{x}$ and μ above, as we try to follow the convention that $\boldsymbol{x}$ is a multi-dimensional random variable and μ is the expectation of the multi-dimensional Gaussian distribution.

For $E[\phi(\xi_{t-1})] = E[\xi_{t-1}\circ\phi(\xi_{t-1})]$, the expectation of a vector function is a vector and each individual element in the resulting vector can be calculated as below. The simple bivariate case was considered

$$\begin{aligned}
E\left[x_1\phi(x_2)\right] &= \int_{-\infty}^{\infty}\int_{-\infty}^{\infty} x_1\phi(x_2)p_2(\boldsymbol{x}|\boldsymbol{\mu},\boldsymbol{\sigma})\mathrm{d}x_1\mathrm{d}x_2\\
&= \frac{1}{\sqrt{2\pi}}\int_{-\infty}^{\infty}\int_{-\infty}^{\infty}\int_{-\infty}^{x_2} x_1\exp\left(-\frac{z^2}{2}\right)p_2(\boldsymbol{x}|\boldsymbol{\mu},\boldsymbol{\sigma})\mathrm{d}z\mathrm{d}x_1\mathrm{d}x_2
\end{aligned} \tag{A6}$$

where p_2 is a bivariate Gaussian distribution for x_1, x_2, and $\boldsymbol{x} = \begin{bmatrix}x_1\\x_2\end{bmatrix}$, $\boldsymbol{\mu} = \begin{bmatrix}\mu_1\\\mu_2\end{bmatrix}$ and $\boldsymbol{\sigma} = \begin{bmatrix}\sigma_{11} & \sigma_{12}\\ \sigma_{21} & \sigma_{22}\end{bmatrix}$ are the expectation and covariance of $\boldsymbol{x}$. We can change the order of integration and shift the $\boldsymbol{z}$ integral (using a change of variable to $\boldsymbol{z}'$) giving

$$E\left[x_1\phi(x_2)\right] = \frac{1}{\sqrt{2\pi}}\int_{-\infty}^{0}\int_{-\infty}^{\infty}\int_{-\infty}^{\infty} x_1\exp\left(-\frac{(z'-x_2)^2}{2}\right)p_2(\boldsymbol{x}|\boldsymbol{\mu},\boldsymbol{\sigma})\mathrm{d}x_2\mathrm{d}x_1\mathrm{d}z' \tag{A7}$$

We expand the quadratic inside the exponent of $\boldsymbol{p}_2(\boldsymbol{x}|\mu,\sigma)$ then collect the x_2 terms inside a single exponent. This gives an integral containing the term of form $\exp(ax_2^2 + bx_2 + c)$, which has the solution

$$\int_{-\infty}^{\infty}\exp(ax_2^2 + bx_2 + c)\mathrm{d}x_2 = \sqrt{\frac{\pi}{-a}\exp\left(c - \frac{b^2}{4a}\right)} \tag{A8}$$

We can solve for the terms a, b, c and substitute back into $E[x_1\phi(x_2)]$ equation, then perform a similar process to collect x_1 terms into the canonical form $x_1\exp(ax_1^2 + bx_1 + c)$. The solution to this second integral is given by

$$\int_{-\infty}^{\infty} x_1\exp(ax_1^2 + bx_1 + c)\mathrm{d}x_1 = b\exp\left(c - \frac{b^2}{4a}\right)\frac{\sqrt{\pi}}{2(-a)^{\frac{3}{2}}}. \tag{A9}$$

Once we solve for these new a, b, c terms and substitute them back into the remaining integral, we can collect the final expression as factors of $\boldsymbol{z}'$ into the form

$$\int_{-\infty}^{0}(d + ez')\exp\left(az'^2 + bz' + c\right)\mathrm{d}z' \tag{A10}$$

This integral can be solved using a combination of two results. The first is

$$d\int_{-\infty}^{0}\exp\left(az'^2 + bz' + c\right)\mathrm{d}z' = d\exp\left(c - \frac{b^2}{4a}\right)\sqrt{\frac{\pi}{-4a}}\left(1 + \mathrm{erf}\left(-\frac{b}{\sqrt{-4a}}\right)\right) \tag{A11}$$

The second solution is

$$e\int_{-\infty}^{0} z'\exp\left(az'^2 + bz' + c\right)\mathrm{d}z' = e\exp\left(c - \frac{b^2}{4a}\right)\frac{\sqrt{-a\pi}b\,\mathrm{erfc}\left(\frac{b}{\sqrt{-4a}}\right) + 2a\exp\left(\frac{b^2}{4a}\right)}{4a^2} \tag{A12}$$

We can combine the above two solutions and simplify to get a general form of the solution for $E[x_1\phi(x_2)]$,

$$E\left[x_1\phi(x_2)\right] = \frac{\mu_1}{2}\mathrm{erf}\left(\frac{\mu_2 - V_0}{\sqrt{2(\sigma_{22}+\varsigma^2)}}\right) + \frac{\mu_1}{2} + \frac{\sigma_{12}}{\sqrt{2\pi(\sigma_{22}+\varsigma^2)}}\exp\left(-\frac{(\mu_2 - V_0)^2}{2(\sigma_{22}+\varsigma^2)}\right) \tag{A13}$$

For $E[\phi(\xi_{t-1})(\xi_{t-1})^\top] = E[\xi_{t-1}\circ\phi(\xi_{t-1})(\xi_{t-1})^\top]$, the individual element in the expectation expression can be written into a trivariate form $E[x_1x_2\phi(x_3)]$. With $\boldsymbol{x}\sim\boldsymbol{p}_3(\boldsymbol{x}|\boldsymbol{\mu},\boldsymbol{\sigma})x\sim p_3(x|\mu,\sigma)$,

$$E\left[x_1\phi(x_2)\right] = \frac{\mu_1}{2}\mathrm{erf}\left(\frac{\mu_2 - V_0}{\sqrt{2(\sigma_{22}+\varsigma^2)}}\right) + \frac{\mu_1}{2} + \frac{\sigma_{12}}{\sqrt{2\pi(\sigma_{22}+\varsigma^2)}}\exp\left(-\frac{(\mu_2 - V_0)^2}{2(\sigma_{22}+\varsigma^2)}\right) \tag{A14}$$

where $\boldsymbol{x} = \begin{bmatrix}x_1\\x_2\\x_3\end{bmatrix}$, $\boldsymbol{\mu} = \begin{bmatrix}\mu_1\\\mu_2\\\mu_3\end{bmatrix}$, $\boldsymbol{\sigma} = \begin{bmatrix}\sigma_{11} & \sigma_{12} & \sigma_{13}\\ \sigma_{21} & \sigma_{22} & \sigma_{23}\\ \sigma_{31} & \sigma_{32} & \sigma_{33}\end{bmatrix}$. The first integral over x_3 takes the canonical form $\int\exp(ax_3^2 + bx_3 + c)\mathrm{d}x_3$, and the second integral over x_2 has a canonical form $\int x_2\exp(ax_2^2 + bx_2 + c)\mathrm{d}x_2$. Those two integrals can be solved with previous solutions above. The third integral over x_1 takes the form $\int(dx_1^2 + ex_1)\exp(ax_1^2 + bx_1 + c)\mathrm{d}x_1$, and can be solved by

$$\int_{-\infty}^{\infty}(dx_1^2 + ex_1)\exp(ax_1^2 + bx_1 + c)\mathrm{d}x_1 = \frac{\sqrt{\pi}}{2(-a)^{\frac{3}{2}}}\left(d - \frac{db^2}{2a} + eb\right)\exp\left(c - \frac{b^2}{4a}\right). \tag{A15}$$

When the coefficients $a-e$ are solved and substituted back in the final integral (in z') has the form and solution

$$\begin{aligned}
&\int_{-\infty}^{0}\left(dz'^2 + ez' + f\right)\exp\left(az'^2 + bz' + c\right)\mathrm{d}z' = \frac{\left(b^2d - 2ad - 2abe + 4a^2f\right)}{8(-a)^{\frac{5}{2}}}\\
&\exp\left(c - \frac{b^2}{4a}\right)\left(1 + \mathrm{erf}\left(-\frac{b}{\sqrt{-4a}}\right)\right) + \frac{2ae - db}{4a^2}\exp(c)
\end{aligned} \tag{A16}$$

After solving for the coefficients $a - f$ and simplifying, the general solution to $E[x_1 x_2 \phi(x_3)]$ is given by

$$E\left[x_1 x_2 \phi(x_3)\right] = \frac{\mu_1\mu_2 + \sigma_{12}}{2}\left(1 + \operatorname{erf}\left(\frac{\mu_3 - V_0}{\sqrt{2(\varsigma^2 + \sigma_{33})}}\right)\right) - \left(\frac{\sigma_{13}\sigma_{23}(\mu_3 - V_0)}{\sqrt{2\pi}(\varsigma^2 + \sigma_{33})^{\frac{3}{2}}} - \frac{\sigma_{23}\mu_1 + \sigma_{13}\mu_2}{\sqrt{2\pi}(\varsigma^2 + \sigma_{33})}\right)\exp\left(\frac{-(\mu_3 - V_0)^2}{2(\varsigma^2 + \sigma_{33})}\right) \tag{A17}$$

In terms of $E[\phi(\xi_{t-1})\phi(\xi_{t-1})^\top] = E[(\xi_{t-1}\circ\phi(\xi_{t-1})\xi_{t-1}\circ\phi(\xi_{t-1}))^\top]$, the terms can be further simplified as $E[\phi(\xi_{t-1})(\phi(\xi_{t-1}))^\top \circ (\xi_{t-1}\xi_{t-1}^\top)]$. An approximation has been made here $E[\phi(\xi_{t-1})(\phi(\xi_{t-1}))^\top \circ (\xi_{t-1}\xi_{t-1}^\top)] = E[\phi(\xi_{t-1})(\phi(\xi_{t-1}))^\top]\circ(\xi_{t-1}\xi_{t-1}^\top)$. The result for the term $E[\phi(\xi_{t-1})(\phi(\xi_{t-1}))^\top]$ can be computed by recognizing that the sigmoid function, ϕ, can be expressed as the Gaussian cumulative distribution function (cdf), with mean V_0 and variance ς. Therefore, the integral can be written as

$$\int_{-\infty}^{\infty}\int_{-\infty}^{\infty}\Phi\left(\frac{x_1 - \mathrm{V}_0}{\varsigma}\right)\Phi\left(\frac{x_2 - \mathrm{V}_0}{\varsigma}\right)\mathrm{p}_2(\boldsymbol{x}|\boldsymbol{\mu},\boldsymbol{\sigma})\mathrm{d}x_1\mathrm{d}x_2 \tag{A18}$$

where $\boldsymbol{x} = \begin{bmatrix} x_1 \\ x_2 \end{bmatrix}$, $\boldsymbol{\mu} = \begin{bmatrix} \mu_1 \\ \mu_2 \end{bmatrix}$, $\boldsymbol{\sigma} = \begin{bmatrix} \sigma_{11} & \sigma_{12} \\ \sigma_{21} & \sigma_{22} \end{bmatrix}$. We define two new, independent random variables, z_1 and z_2 that are both normally distributed with mean, V_0 and variance, ς. As z_1 and z_2 are independent of x_1 and x_2, we have

$$P(z_1 < x_1, z_2\langle x_2|x_1, x_2) = \Phi\left(\frac{x_1 - \mathrm{V}_0}{\varsigma}\right)\Phi\left(\frac{x_2 - \mathrm{V}_0}{\varsigma}\right) \tag{A19}$$

and by the law of total probability, the unconditional distribution is calculated by

$$\begin{aligned} P(z_1 < x_1, z_2 < x_2) &= \int_{-\infty}^{\infty}\int_{-\infty}^{\infty} P(z_1 < x_1, z_2\langle x_2|x_1, x_2)\mathrm{p}_2(\boldsymbol{x}|\boldsymbol{\mu},\boldsymbol{\sigma})\mathrm{d}x_1\mathrm{d}x_2 \\ &= P(z_1 - x_1 < 0, z_2 - x_2 < 0) \\ &= \Phi\left(\frac{\boldsymbol{z} - \hat{\boldsymbol{\mu}}}{\hat{\boldsymbol{\sigma}}}\right) \end{aligned} \tag{A20}$$

$\Phi(\frac{\boldsymbol{z}-\hat{\boldsymbol{\mu}}}{\hat{\boldsymbol{\sigma}}})$ is a bivariate Gaussian cdf, with $\boldsymbol{z} = \begin{bmatrix} z_1 \\ z_2 \end{bmatrix}$, $\hat{\boldsymbol{\mu}} = \begin{bmatrix} \hat{\mu}_1 \\ \hat{\mu}_2 \end{bmatrix}$, and $\hat{\boldsymbol{\sigma}} = \begin{bmatrix} \hat{\sigma}_{11} & \hat{\sigma}_{12} \\ \hat{\sigma}_{21} & \hat{\sigma}_{22} \end{bmatrix}$. These terms can be calculated by recognizing

$$\begin{aligned} \hat{\mu}_1 &= E\left[z_1 - x_1\right] = \mathrm{V}_0 - \mu_1 \\ \hat{\mu}_1 &= E\left[z_1 - x_1\right] = \mathrm{V}_0 - \mu_1 \\ \hat{\sigma}_{11} &= \mathrm{var}\left(z_1 - x_1\right) = \varsigma^2 + \sigma_{11} \\ \hat{\sigma}_{22} &= \mathrm{var}\left(z_2 - x_2\right) = \varsigma^2 + \sigma_{22} \\ \hat{\sigma}_{12} &= \hat{\sigma}_{21} = \mathrm{cov}\left(z_1 - x_1, z_2 - x_2\right) = \sigma_{12} \end{aligned} \tag{A21}$$

References

Aarabi, A., He, B., 2014. Seizure prediction in hippocampal and neocortical epilepsy using a model-based approach. Clin. Neurophysiol. 125, 930–940.

Abeysuriya, R., Robinson, P., 2016. Real-time automated EEG tracking of brain states using neural field theory. J. Neurosci. Methods 258, 28–45.

Aquino, K.M., Robinson, P.A., Schira, M.M., Breakspear, M., 2014. Deconvolution of neural dynamics from fMRI data using a spatiotemporal hemodynamic response function. Neuroimage 94, 203–215.

Beckmann, C.F., DeLuca, M., Devlin, J.T., Smith, S.M., 2005. Investigations into resting-state connectivity using independent component analysis. Philos. Trans. R. Soc. B 360, 1001–1013.

Breakspear, M., 2017. Dynamic models of large-scale brain activity. Nat. Neurosci. 20, 340–352.

Brookes, M.J., Woolrich, M., Luckhoo, H., Price, D., Hale, J.R., Stephenson, M.C., Barnes, G.R., Smith, S.M., Morris, P.G., 2011. Investigating the electrophysiological basis of resting state networks using magnetoencephalography. Proc. Natl. Acad. Sci. 108, 16783–16788.

Cohen, M.X., 2017. Where does EEG come from and what does it mean? Trends Neurosci. 40, 208–218.

Cuevas, E., Echavarría, A., Ramírez-Ortegón, M.A., 2014. An optimization algorithm inspired by the States of Matter that improves the balance between exploration and exploitation. Appl. Intell. 40, 256–272.

Daunizeau, J., David, O., Stephan, K.E., 2011. Dynamic causal modelling: a critical review of the biophysical and statistical foundations. Neuroimage 58, 312–322.

David, O., Friston, K.J., 2003. A neural mass model for MEG/EEG:: coupling and neuronal dynamics. Neuroimage 20, 1743–1755.

David, O., Kiebel, S.J., Harrison, L.M., Mattout, J., Kilner, J.M., Friston, K.J., 2006. Dynamic causal modeling of evoked responses in EEG and MEG. Neuroimage 30, 1255–1272.

Deco, G., Jirsa, V.K., Robinson, P.A., Breakspear, M., Friston, K., 2008. The dynamic brain: from spiking neurons to neural masses and cortical fields. PLoS Comput. Biol. 4, e1000092.

Einevoll, G., 2021. Modeling EEG Signals From the Bottom Up. Int. J. Psychophysiol. 168, S14–S15.

Escuain-Poole, L., Garcia-Ojalvo, J., Pons, A.J., 2018. Extracranial estimation of neural mass model parameters using the unscented Kalman filter. Front. Appl. Math. Stat. 4, 46.

Farras-Permanyer, L., Mancho-Fora, N., Montalà-Flaquer, M., Bartrés-Faz, D., Vaqué-Alcázar, L., Peró-Cebollero, M., Guàrdia-Olmos, J., 2019. Age-related changes in resting-state functional connectivity in older adults. Neural Regen. Res. 14, 1544.

Frässle, S., Lomakina, E.I., Razi, A., Friston, K.J., Buhmann, J.M., Stephan, K.E., 2017. Regression DCM for fMRI. Neuroimage 155, 406–421.

Freestone, D.R., Aram, P., Dewar, M., Scerri, K., Grayden, D.B., Kadirkamanathan, V., 2011. A data-driven framework for neural field modeling. Neuroimage 56, 1043–1058.

Freestone, D.R., Karoly, P.J., Nešić, D., Aram, P., Cook, M.J., Grayden, D.B., 2014. Estimation of effective connectivity via data-driven neural modeling. Front. Neurosci. 8, 383.

Freestone, D.R., Layton, K.J., Kuhlmann, L., Cook, M.J., 2017. Statistical performance analysis of data-driven neural models. Int. J. Neural Syst. 27, 1650045.

Freyer, F., Roberts, J.A., Becker, R., Robinson, P.A., Ritter, P., Breakspear, M., 2011. Biophysical mechanisms of multistability in resting-state cortical rhythms. J. Neurosci. 31, 6353–6361.

Friston, K.J., 2002. Bayesian estimation of dynamical systems: an application to fMRI. Neuroimage 16, 513–530.

Friston, K.J., Harrison, L., Penny, W., 2003. Dynamic causal modelling. Neuroimage 19, 1273–1302.

Friston, K.J., Holmes, A.P., Worsley, K.J., Poline, J.P., Frith, C.D., Frackowiak, R.S., 1994. Statistical parametric maps in functional imaging: a general linear approach. Hum. Brain Mapp. 2, 189–210.

Friston, K.J., Preller, K.H., Mathys, C., Cagnan, H., Heinzle, J., Razi, A., Zeidman, P., 2019. Dynamic causal modelling revisited. Neuroimage 199, 730–744.

Galka, A., Yamashita, O., Ozaki, T., Biscay, R., Valdés-Sosa, P., 2004. A solution to the dynamical inverse problem of EEG generation using spatiotemporal Kalman filtering. Neuroimage 23, 435–453.

Georgieva, A., Jordanov, I., 2009. Global optimization based on novel heuristics, low-discrepancy sequences and genetic algorithms. Eur. J. Oper. Res. 196, 413–422.

Gonçalves, S.I., De Munck, J.C., Pouwels, P.J., Schoonhoven, R., Kuijer, J.P., Maurits, N.M., Hoogduin, J.M., Van Someren, E.J., Heethaar, R.M., Da Silva, F.L., 2006. Correlating the alpha rhythm to BOLD using simultaneous EEG/fMRI: inter-subject variability. Neuroimage 30, 203–213.

Grimbert, F., Faugeras, O., 2006. Bifurcation analysis of Jansen's neural mass model. Neural Comput. 18, 3052–3068.

Halgren, M., Ulbert, I., Bastuji, H., Fabó, D., Erőss, L., Rey, M., Devinsky, O., Doyle, W.K., Mak-McCully, R., Halgren, E., 2019. The generation and propagation of the human alpha rhythm. Proc. Natl. Acad. Sci. 116, 23772–23782.

Handwerker, D.A., Ollinger, J.M., D'Esposito, M., 2004. Variation of BOLD hemodynamic responses across subjects and brain regions and their effects on statistical analyses. Neuroimage 21, 1639–1651.

Hartoyo, A., Cadusch, P.J., Liley, D.T., Hicks, D.G., 2019. Parameter estimation and identifiability in a neural population model for electro-cortical activity. PLoS Comput. Biol. 15, e1006694.

Hashemi, M., Hutt, A., Buhry, L., Sleigh, J., 2018. Optimal model parameter estimation from EEG power spectrum features observed during general anesthesia. Neuroinformatics 16, 231–251.

Hashemi, M., Vattikonda, A.N., Sip, V., Diaz-Pier, S., Peyser, A., Wang, H., Guye, M., Bartolomei, F., Woodman, M.M., Jirsa, V.K., 2021. On the influence of prior information evaluated by fully Bayesian criteria in a personalized whole-brain model of epilepsy spread. PLoS Comput. Biol. 17, e1009129.

Higham, N.J., 1988. Computing a nearest symmetric positive semidefinite matrix. Linear Algebra Appl. 103, 103–118.

Hillebrand, A., Barnes, G.R., Bosboom, J.L., Berendse, H.W., Stam, C.J., 2012. Frequency-dependent functional connectivity within resting-state networks: an atlas-based MEG beamformer solution. Neuroimage 59, 3909–3921.

Hipp, J.F., Hawellek, D.J., Corbetta, M., Siegel, M., Engel, A.K., 2012. Large-scale cortical correlation structure of spontaneous oscillatory activity. Nat. Neurosci. 15, 884–890.

Hoover, E.E., Squier, J.A., 2013. Advances in multiphoton microscopy technology. Nat. Photonics 7, 93–101.

Jansen, B.H., Rit, V.G., 1995. Electroencephalogram and visual evoked potential generation in a mathematical model of coupled cortical columns. Biol. Cybern. 73, 357–366.

Kalman, R.E., 1960. A new approach to linear filtering and prediction problems.

Kandel, E.R., Schwartz, J.H., Jessell, T.M., Siegelbaum, S., Hudspeth, A.J., Mack, S., 2000. Principles of Neural Science. McGraw-hill, New York.

Karoly, P.J., Kuhlmann, L., Soudry, D., Grayden, D.B., Cook, M.J., Freestone, D.R., 2018. Seizure pathways: a model-based investigation. PLoS Comput. Biol. 14, e1006403.

Kiebel, S.J., Garrido, M.I., Friston, K.J., 2007. Dynamic causal modelling of evoked responses: the role of intrinsic connections. Neuroimage 36, 332–345.
Kiebel, S.J., Garrido, M.I., Moran, R.J., Friston, K.J., 2008. Dynamic causal modelling for EEG and MEG. Cogn. Neurodyn. 2, 121–136.
Klimesch, W., Sauseng, P., Hanslmayr, S., 2007. EEG alpha oscillations: the inhibition—timing hypothesis. Brain Res. Rev. 53, 63–88.
Kuhlmann, L., Freestone, D.R., Manton, J.H., Heyse, B., Vereecke, H.E., Lipping, T., Struys, M.M., Liley, D.T., 2016. Neural mass model-based tracking of anesthetic brain states. Neuroimage 133, 438–456.
Lamus, C., Hämäläinen, M.S., Temereanca, S., Brown, E.N., Purdon, P.L., 2012. A spatiotemporal dynamic distributed solution to the MEG inverse problem. Neuroimage 63, 894–909.
Li, B., Daunizeau, J., Stephan, K.E., Penny, W., Hu, D., Friston, K., 2011. Generalised filtering and stochastic DCM for fMRI. Neuroimage 58, 442–457.
Liley, D.T., Cadusch, P.J., Dafilis, M.P., 2001. A spatially continuous mean field theory of electrocortical activity. Network: Comput. Neural Syst. 13, 67.
Liu, X., Gao, Q., 2013. Parameter estimation and control for a neural mass model based on the unscented Kalman filter. Phys. Rev. E 88, 042905.
Logothetis, N.K., 2003. The underpinnings of the BOLD functional magnetic resonance imaging signal. J. Neurosci. 23, 3963–3971.
Logothetis, N.K., Pauls, J., Augath, M., Trinath, T., Oeltermann, A., 2001. Neurophysiological investigation of the basis of the fMRI signal. Nature 412, 150–157.
Lozano-Soldevilla, D., 2018. On the physiological modulation and potential mechanisms underlying parieto-occipital alpha oscillations. Front. Comput. Neurosci. 12, 23.
Marreiros, A.C., Kiebel, S.J., Daunizeau, J., Harrison, L.M., Friston, K.J., 2009. Population dynamics under the Laplace assumption. Neuroimage 44, 701–714.
Mukherjee, P., Berman, J., Chung, S., Hess, C., Henry, R., 2008. Diffusion tensor MR imaging and fiber tractography: theoretic underpinnings. Am. J. Neuroradiol. 29, 632–641.
Nichols, T.E., Holmes, A.P., 2002. Nonparametric permutation tests for functional neuroimaging: a primer with examples. Hum. Brain Mapp. 15, 1–25.
Novotny Jr, E.J., Fulbright, R.K., Pearl, P.L., Gibson, K.M., Rothman, D.L., 2003. Magnetic resonance spectroscopy of neurotransmitters in human brain. Ann. Neurol. 54, S25–S31.
Nunez, P.L., Srinivasan, R., 2006. Electric Fields of the brain: the Neurophysics of EEG. Oxford University Press, USA.
Oostenveld, R., Fries, P., Maris, E., Schoffelen, J.-M., 2011. FieldTrip: open source software for advanced analysis of MEG, EEG, and invasive electrophysiological data. Comput. Intell. Neurosci. 2011.
Pelentritou, A., Kuhlmann, L., Cormack, J., Mcguigan, S., Woods, W., Muthukumaraswamy, S., Liley, D., 2020. Source-level cortical power changes for xenon and nitrous oxide–induced reductions in consciousness in healthy male volunteers. Anesthesiology 132, 1017–1033.
Pelentritou, A., Kuhlmann, L., Cormack, J., Woods, W., Sleigh, J., Liley, D., 2018. Recording brain electromagnetic activity during the administration of the gaseous anesthetic agents xenon and nitrous oxide in healthy volunteers. JoVE (J. Vis. Exp.) e56881.
Penny, W.D., Friston, K.J., Ashburner, J.T., Kiebel, S.J., Nichols, T.E., 2011. Statistical Parametric mapping: the Analysis of Functional Brain Images. Elsevier.
Penny, W.D., Stephan, K.E., Mechelli, A., Friston, K.J., 2004. Comparing dynamic causal models. Neuroimage 22, 1157–1172.
Prando, G., Zorzi, M., Bertoldo, A., Corbetta, M., Zorzi, M., Chiuso, A., 2020. Sparse DCM for whole-brain effective connectivity from resting-state fMRI data. Neuroimage 208, 116367.
Ritter, P., Schirner, M., McIntosh, A.R., Jirsa, V.K., 2013. The virtual brain integrates computational modeling and multimodal neuroimaging. Brain Connect. 3, 121–145.
Ruxton, G.D., 2006. The unequal variance *t*-test is an underused alternative to Student's *t*-test and the Mann–Whitney U test. Behav. Ecol. 17, 688–690.
Schiff, S.J., 2012. Neural Control engineering: the Emerging Intersection Between Control Theory and Neuroscience. MIT Press.
Simon, D., 2006. Optimal State estimation: Kalman, H infinity, and Nonlinear Approaches. John Wiley & Sons.
Tagliazucchi, E., Von Wegner, F., Morzelewski, A., Brodbeck, V., Laufs, H., 2012. Dynamic BOLD functional connectivity in humans and its electrophysiological correlates. Front. Hum. Neurosci. 6, 339.
Van de Steen, F., Almgren, H., Razi, A., Friston, K., Marinazzo, D., 2019. Dynamic causal modelling of fluctuating connectivity in resting-state EEG. Neuroimage 189, 476–484.
Van Veen, B.D., Van Drongelen, W., Yuchtman, M., Suzuki, A., 1997. Localization of brain electrical activity via linearly constrained minimum variance spatial filtering. IEEE Trans. Biomed. Eng. 44, 867–880.
Welch, B.L., 1947. The generalization of 'STUDENT'S'problem when several different population varlances are involved. Biometrika 34, 28–35.
Wendling, F., Bartolomei, F., Bellanger, J., Chauvel, P., 2002. Epileptic fast activity can be explained by a model of impaired GABAergic dendritic inhibition. Eur. J. Neurosci. 15, 1499–1508.
Worsley, K.J., Evans, A.C., Marrett, S., Neelin, P., 1992. A three-dimensional statistical analysis for CBF activation studies in human brain. J. Cereb. Blood Flow Metabol. 12, 900–918.
Worsley, K.J., Marrett, S., Neelin, P., Vandal, A.C., Friston, K.J., Evans, A.C., 1996. A unified statistical approach for determining significant signals in images of cerebral activation. Hum. Brain Mapp. 4, 58–73.